NTNU – Trondheim
Norwegian University of
Science and Technology

Analysis of a Novel Coil Design for Axial Flux Machines

Sigbjørn Lomheim

Master of Energy and Environmental Engineering
Submission date: June 2013
Supervisor: Robert Nilssen, ELKRAFT

Norwegian University of Science and Technology
Department of Electric Power Engineering

Problem Description

This master thesis will be a continuation of the specialization project “Investigation of a Novel Coil Design Suited for Axial Flux Permanent Magnet Machines” from fall semester 2013.

A novel coil design for axial flux electric machines is to be studied and analyzed. Analytical models are to be developed and tested through simulations in Matlab and FEM-tools. A prototype stator is to be designed according to the electric motor in the NTNUs Shell Eco Marathon team. The prototype shall be manufactured and tested in laboratory to investigate its performance and characteristics, and proving that this coil design can successfully be built and work as an electric motor.

In parallel to this thesis, a lab experiment is conducted by Lars Johan Clad at the Department of Energy and Process Engineering in effort to find the cooling capability of this coil design, and reported in his thesis: “Cooling Systems for High Energy Efficient Electric Motors”.

Supervisors:
Prof. Robert Nilssen
Dr. Jon Eirik Brennvall

Preface

Today the electrical motors are embedded in almost every market segment in the industry, providing a smarter, safer and efficient alternative to cope with the work load. However, there are a number of areas where the electric motor has yet to be introduced.

A difficult challenge to the electric motor is to compete with hydraulic motors, where the torque density requirement is beyond any machine design today. In order to build a torque dense electrical machine, the geometrical dimensions must be small while the current densities are high, which results in a low efficient machine. The low efficiency implies that the machine has high losses, and must be very efficiently cooled. In effort to build such a machine, a novel coil design has been developed by Dr. Jon Eirik Brennvall at Greenway Energy AS. This master thesis work has been to study this design, identifying how such a machine can be made, and how it performs in an industrial application.

I would like give my sincere gratitude and thanks to my supervisors: Prof. Robert Nilssen and Dr. Jon Eirik Brennvall, who gave me the opportunity to write this master thesis. Their help and support though this year has been invaluable to finish my work.

I am grateful for the founding from Greenway Energy AS to build the stator prototype, and a special thanks to Øystein Hagemo at Finmekanisk Verksted in Realfagsbygget who did a remarkable job to manufacture the prototype.

My work could not have been done if not for the help and advices from PhD students Astrid Røkke and Zhang Zhao Qiang. The support from the service lab and the workshop has been crucial to the completion of the prototype, and I would like to give a special thanks to Bård Almås, Kurt Salmi, Dominik Häger, Erland Strendo, and Oddvar Landrø, for their advices and help in difficult situations.

At last I would like to give a special thanks to my beloved girlfriend, who has supported me through my work, helping me to keep my moral and strength, and allowing me to devote my time to this thesis.

Sigbjørn Lomheim
Department of Electric Power Engineering
Norwegian University of Science and Technology
Trondheim, Norway
23rd June 2013

Norsk Samandrag

I denne oppgåva blir eit nytt spoledesign for permanentmagnet aksialfluks maskinar presentert. Ein analyse av maskinens evne til å operere, med tanke på spolelegging, kjøleevne, koggingmoment, og indusert spenning, er gjennomført. Forskjellige metodar for å tilverke og montere spoledesigne er presentert. Ein stator prototype er bygget og testa, der det endelige resultatet viser at den har ein fyllfaktor på 90%. Prototypen er bygd som ein jernfri bølgjevikla stator, og er blitt studert ved hjelp av analytiske modellar og testing i laboratorium. Ein analyse av effekten av å introdusere jern i designe er gjennomført. Ein analytisk modell som beskriver ytinga til motoren med jernstator er laget og presentert i denne oppgåva. Jernmodellen er så brukt til å forutseia designets yting i forskjellige applikasjonar der høgt moment og lavt turtall trengs. Det viser seg at dette designet realiserar høg momenttettheit, men kombinasjonen mellom liten fysisk størrelse og høg straumtettheit, vil verknadsgraden bli lav, og liggje i området mellom 30 og 40%. Ein undersøking av kjøleeigenskapane til dette spoledesignet er gjennomført av master studenten Lars Johan Clad, frå institutt for energi- og prosessteknikk [1]. Her blir det bevist at kjølinga med dette spoledesignet kan kjøre ein straumtettheit på 20A/mm^2, med kun 60° arbeidstemperatur på spolen.

Analysis of a Novel Coil Design for Axial Flux Machines

Sigbjørn Lomheim
Norwegian University of Science and Technology
Department of Electrical Power Engineering
Trondheim June 23, 2013

***Abstract*—A novel coil design for permanent magnet axial flux machines is presented. An analysis of its performance regarding winding layout, cooling capability, cogging torque, and back-EMF is conducted. Different manufacturing and assembly methods are described. A prototype stator has been built and tested. The prototype stator has a 90% fill factor, and is an iron free wave-winded topology. The prototype has been analyzed using analytical approaches, and compared to the performance in the laboratory testing. An analysis of introducing iron in the stator has been done, where the effect of iron stator is compared to the iron free prototype. An analytical model describing the performance of the iron stator has been developed and presented in this thesis. The model is used to present its performance in industrial applications, where high torque - low speed properties are needed. The results show that this design may compete with hydraulic motors in the industry, having an extremely high torque density, but due to high current densities, an efficiency of 30% to 40%. An investigation of the cooling capability of the coil design has been conducted by master student Lars Johan Clad at the Department of Energy and Process Engineering at NTNU[1]. It has here been proved that the cooling of this coil design is sufficient to enable a current density of $20A/mm^2$ in the stator conductors, with only 60° operating temperature.**

I. Introduction

Focus on high efficiency and invention of high performance permanent magnets (PMs) has "reinvented" their use in electric machines today. A high magnetic remanence and demagnetization capabilities makes it possible to replace the field-winding in brushless synchronous machines, resulting in a compact machine design with high efficiency and performance. The axial flux brushless PM machine (AFPM) has gained significant interest due to this, and opened a broad application variety within all power ranges [3][7].

The maximum energy density of rare-earth PMs has been steadily increasing since their invention in the 1980s, and is expected to increase further. The cost of PMs has at the same time decreased, and widened their use in electrical machinery. During the recent years, the Chinese has gained a monopolistic position in exporting rare-earth metals like neodymium, and in 2011 the export was decreased creating a shortage. The monopolistic position and shortage contribute to a unstable price development in the future, with higher cost and fluctuations[8].

In AFPMs, the PM material represents the largest contributor to its bill of materials[4]. As seen in the motor manufacture industry, cost per machine in a mass production is asymptotically reduced to the bill of materials giving the absolute minimum manufacturing cost[3]. Having an unstable price development gives an uncertainty, which makes it harder to adopt the AFPM in the industry.

II. Radial- versus axial flux electrical machines

The difference between radial and axial flux machines lies in their names; the radial flux machine use radial directed magnetic flux established on the rotor which interacts with stator current to produce electromagnetic torque. The axial flux machine has axial directed magnetic flux which interacts with stator current to produce torque. The strength of the force producing the torque is given by (1)

$$\vec{F} = q\vec{v} \times \vec{B} \tag{1}$$

where $\vec{F}$ is the force resulting from the magnetic field $\vec{B}$ acting on current $q\vec{v}$. In an electrical machine the force is acting in the circumferential direction, which means that the current and magnetic fields are confined to the radial and axial directions which lead to the two machine types.

The axial flux machine is not a new discovery, the first working prototype was built by M. Faraday in 1831 [9]. But due to the complexity in mechanical design, difficulty to maintain a uniform airgap, and poor quality PMs, made the radial flux counterpart a more cost effective motor and has been the number one choice since its introduction in 1837 patented by inventor T. Davenport. After the invention of high quality PMs in the 1980s, the AFPM is now proven to be cost effective, and challenging its radial flux counterpart in a number of areas[3]. The advantage of the axial flux machine is the possibility to design a very compact disc shaped motor, with high torque per volume.

$$T_{radial} = kD^2L \tag{2}$$

$$T_{axial} = kD^3 \tag{3}$$

The machine torque sizing equations for a radial flux compared to axial flux is given by (2) and (3) respectively, where k is the machine constant used to compare sizing of equal designed machines, D is the diameter of rotor, and L is the length of the machine[2]. The key difference between axial flux and radial flux is that the radial flux machine can be scaled by adjusting the length of the machine, while the axial flux has an optimized machine length for a given

diameter. The diameter of an axial flux machine has its mechanical limitations, where increasing the diameter results in higher torque while the contact surface to the shaft joint is constant[9]. Because of this, the scaling of an axial flux machine is done by having multiple discs when maximum diameter is reached. When the radial flux machine is scaled with length, the end coil volume remains the same, while an axial flux machine has the same amount of end coil in each inserted disc, giving the radial flux an advantage in high torque applications. It is proven that the axial flux design can be used in the high speed-high torque power ranges, and is up to four times lighter and much smaller than its radial counterpart at equal rating[7].

III. Axial-flux topologies

Within axial flux machines there exists a wide variety of how to utilize the axial magnetic field to produce torque. There are advantages and drawbacks for each topology, and the choice of which topology to use is dependent on the application of the machine. Only the axial flux topologies of the disc machine are presented here, the transverse flux is not included but can be found in literature[2][9].

Single Sided AFPM

The most intuitive topology is the single sided axial flux machine seen in Fig. 1. Only one disc contains magnets, which is the rotor, and one disc contains coils, stator. The magnets are placed on the rotor alternating between north and south pole to face the stator as shown in Fig. 5. The machine consists of few parts, and offers a low-cost and compact design. Due to the single sided rotor, the axial attractive forces between rotor and stator are not canceled out. Because of the disc geometry the force may bend the rotor discs. Therefore the discs need mechanical support and strong bearings. The single sided design requires back iron in the stator as well as the rotor to achieve suitable air-gap flux density and high flux-linkage between magnet and coil. The stator back iron will be a part of the machine housing, providing an effective heat-flux path to cool the machine. An example of a commercial machine with this topology is the Finnish elevator company *KONE Inc*, where this design is used to mount the elevator propulsion system directly on the elevator.

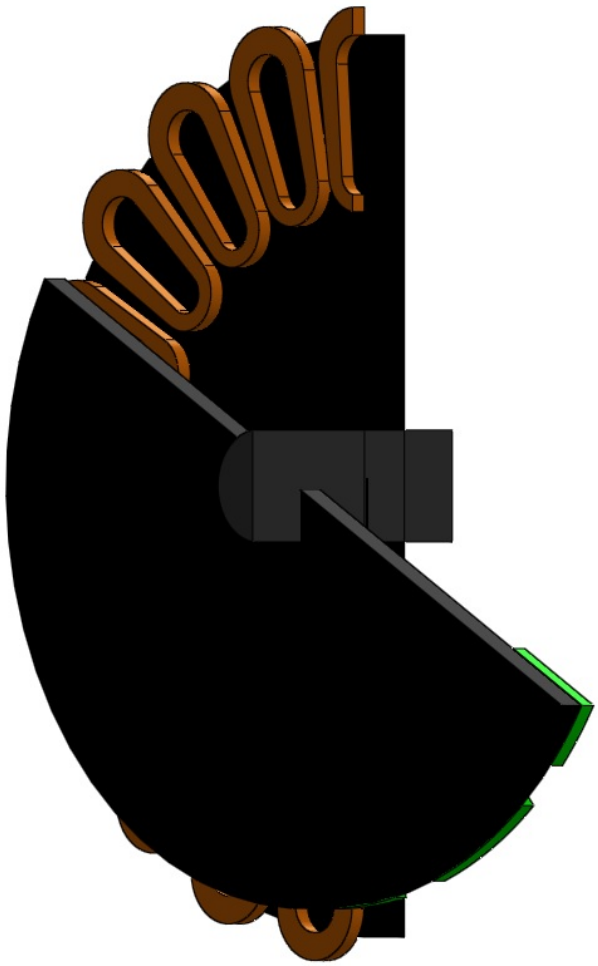

Fig. 1: Single Sided AFPM

Double Sided AFPM - Internal stator

In the double sided internal stator axial flux design, the stator is sandwiched between two rotors discs. An example of this is shown in Fig. 2. The magnets are laid on each rotor the same way as for the single sided topology, but having a north-south relation between the rotors so the flux is passing from one magnet to the other before turning back, as shown in Fig. 6. The advantage for this topology, compared to the latter, is the cancellation of axial force acting on the stator.

The double sided design allows the internal stator disc to be iron free, as the flux is directed through the stator by magnets on both sides. Removing the stator iron is increasing the active air-gap length, and larger magnets are needed which increases costs. The stator can be supported by reinforced epoxy resin or similar material which does not have magnetic or electric conductivity, thereby removing stator iron losses and cogging torque. This iron-free stator topology is used in the newly developed 10MW Sway generator from Smart Motor AS.

The heat removal from this design is more difficult than in the latter design, because the stator coils are situated sandwiched between rotating parts. The stator may be cooled by directing air flow radially in the air-gap, which happens naturally when the machine is rotating. The cooling can be increased by external fans or introduce water cooling channels inside the stator.

By assembling the rotor magnets in a ”Halbach array” shown in Fig. 8, the rotor back iron which is used to turn the magnetic flux, may be discarded. Doing this will remove the need for magnetic iron in the machine, which in turn reduces the losses in the machine significantly. By removing the magnetic iron in both stator and rotor eliminates most of the parasitic forces, and the Halbach array provides a nearly sinusoidal air-gap flux which in turn reduces the harmonic losses. This topology is used in the DNV - fuel fighter, which on behalf of NTNU participates in the Shell Eco-

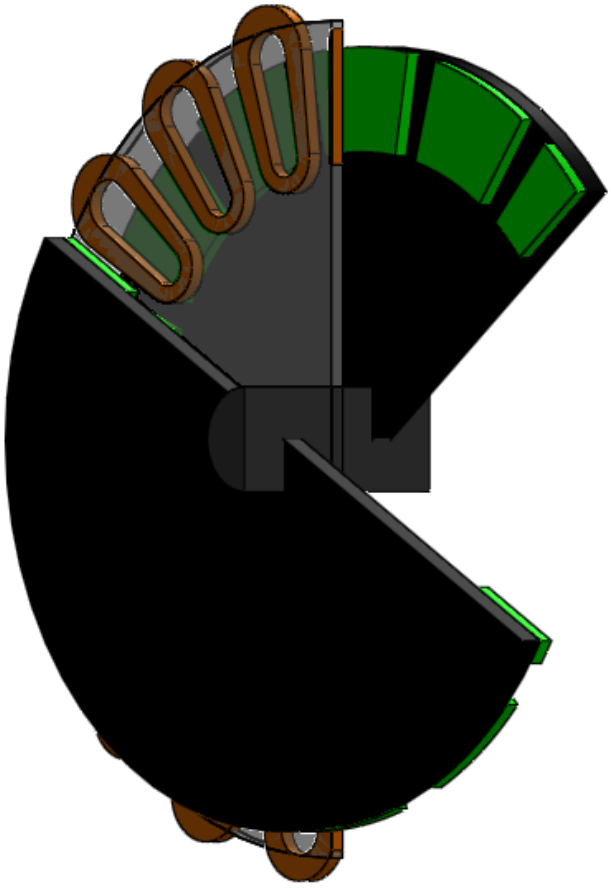

Fig. 2: Double Sided internal stator AFPM

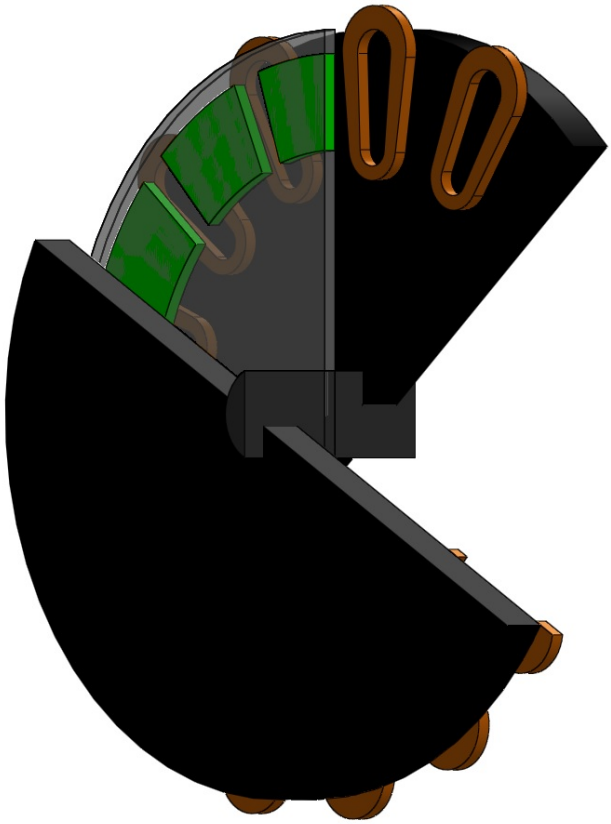

Fig. 3: Double Sided internal rotor AFPM

marathon competition. The advantage of having an iron free machine is very high efficiency and very low weight[11]. The disadvantage of using Halbach array and ironless stator is the increased amount of PMs, resulting in a very costly machine. Therefore, this iron free topology is suitable for high performance applications.

Double sided AFPM - Internal rotor

Instead of having the stator in the middle, the rotor is now sandwiched between two stator discs as seen in Fig. 3. The stator must contain back-iron to provide a magnetic flux path as the single sided AFPM. Having stators positioned at the ends will conceal and protect the rotor, and eliminate the need for a separate housing. Because of this, the heat removal from the stator coils is much easier, where they are in direct contact with the machine frame, and provide a good heat flux path to the outer surface.

Multidisc AFPM

When the machine diameter is mechanically constrained, it is possible to insert more discs in series to gain higher torque. The magnetic flux passes through all discs before turning back, meaning that only the end discs need magnetic back iron to direct the flux through the machine. The interior discs can be iron free as discussed in the latter two topologies. Introducing more discs will not increase the efficiency of the machine, because the torque versus losses in each rotor-stator section will be the same. Also, the end coil volume for each disc will remain the same, and at some point it will be preferable to use the radial flux machine because of its constant end coil volume for any length. In Fig. 4 a multidisc internal stator topology is shown.

Rotor assembly options

In brushless axial flux machines, the PMs are placed on the rotor alternating between north- and south-pole facing up. One magnet represenst one rotor pole, and the pole pitch τ_p is the circumferential distance between each pole, while the magnet pitch τ_m is the circumferential span of the magnet as seen in Fig. 5. The magnets are glued to the back iron, and can withstand very high mechanical forces. Usually, the magnets are laid with a certain distance to the next magnet, due to magnet to magnet leakage flux. In Fig. 6 a 2D-sheet of a double sided internal stator axial flux machine is shown. It represents a circumferential 2D-sheet at a constant radius over two pole pitches. The magnetic flux lines produced from the rotor magnets are shown, and the magnet to magnet leakage flux can be seen as not crossing the air-gap.

The magnets can be glued on top of the back-iron as described, but to increase the mechanical strength it can be ”buried” in the iron. The lower rotor in Fig. 7 is showing

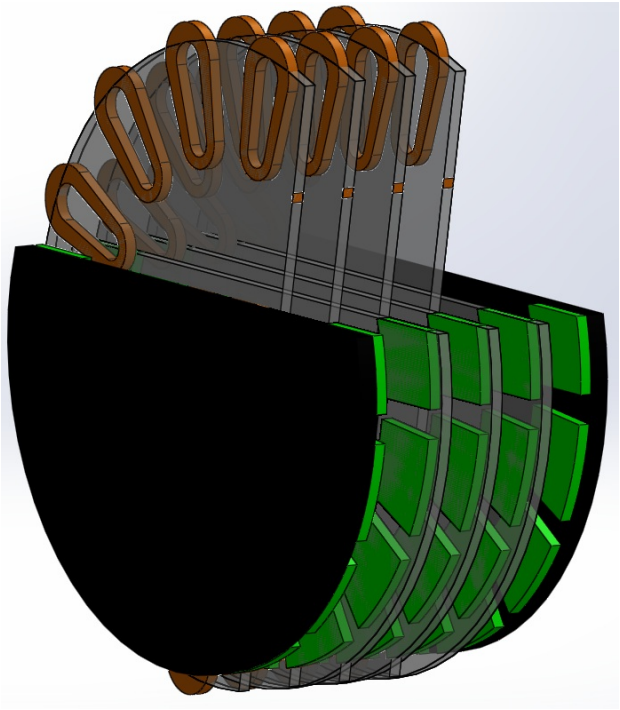

Fig. 4: Multidisc internal stator AFPM

magnets partially buried in the back-iron. This increases the mechanical strength of the magnet, but also increases the the flux leakage. In the upper rotor par,t a different rotor topology is used. Here, the magnets are completely buried in the back-iron and are shifted to magnetize in the circumferential direction. This method is used to gain higher air-gap flux. This happens when the magnet surface is larger than the air-gap surface. This is expressed as

$$B_g = \frac{A_m}{A_g} B_m \tag{4}$$

where A_g is the air-gap surface, A_m is the magnet surface, B_g is the air-gap flux density, and B_m is the magnet flux density. This is a common method to achieve sufficient air-gap flux density with low quality magnets.

The torque generated by the machine is dependent on variation in inductance, and from coenenergy the torque equation dependent on inductances is [2]

$$T = \frac{1}{2} i_1^2 \frac{dL}{d\theta} - \frac{1}{2} \phi_m^2 \frac{dR}{d\theta} + N i_1 \frac{d\phi_m}{d\theta} \tag{5}$$

where i_1 is the stator phase current, L is the stator coil inductance, ϕ_m is the flux produced by the magnet, and R is the magnetic reluctance seen by the magnet.

The first term is the reluctance torque, which occurs when the coil inductance vary with position. This happens in rotor designs with saliency or embedded magnets in the rotor back iron. In Fig. 6, the coil inductance is constant for any rotor position, hence zero reluctance torque. In Fig. 7, the magnets are buried into the rotor back iron. Because of variation in the

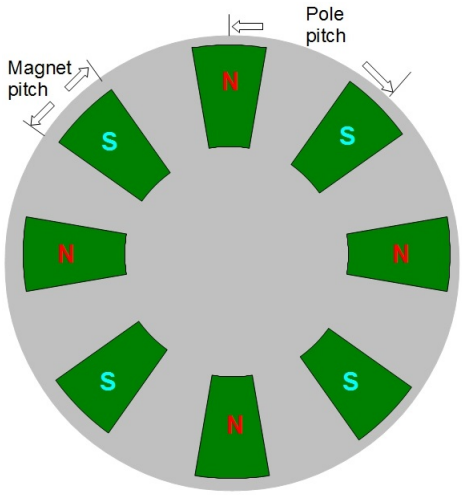

Fig. 5: Magnet poles on rotor

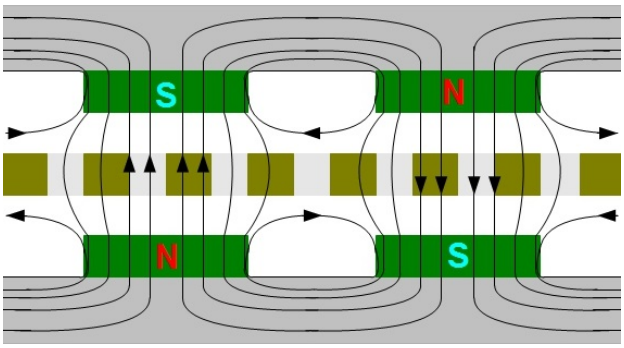

Fig. 6: 2D sheet of double sided internal stator AFPM

magnetic resistance for different rotor position, the reluctance torque term is not zero. To have variable magnetic reluctance in the rotor is often an advantage. The d- and q-inductances for the stator are dependent on the rotor magnetic reluctance, and to have a high L_d compared to L_q will provide flux weakening capability, which is the case in the lower rotor part in Fig. 7. The second term is the magnet reluctance torque, called cogging torque, which occurs when iron is introduced in the stator design. Teeth in a slotted iron stator provide a variable air-gap magnetic reluctance which cause vibration and noise to the machine. The last term is the mutual torque, which is the torque producing equation in synchronous and asynchronous machines. The design process of such machines should minimize the first two terms in (5) as they are considered parasitic torque components which produce a ripple in the output power.

In Fig. 8, a typical Halbach array is shown. Instead of having back iron, the flux lines are directed and turned by magnets, and resulting in an iron free machine. The amount of magnets in this rotor topology is higher since the magnets are placed back to back, filling up the entire pole pitch. Also, larger magnets are needed to be able to handle the amount of magnetic flux passing through them. It is possible to have 60° or 45° shifted magnets, resulting in a higher air-gap flux

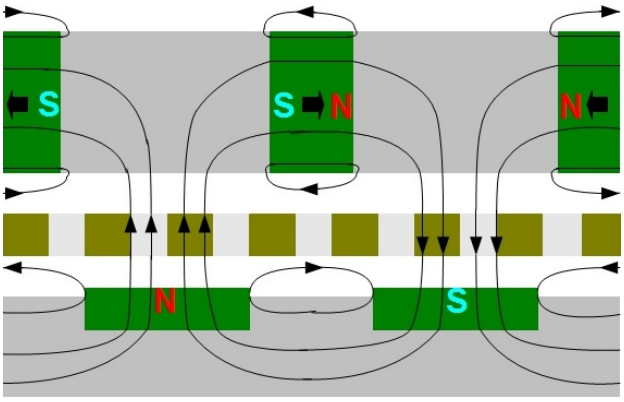

Fig. 7: Buried Rotor Magnets

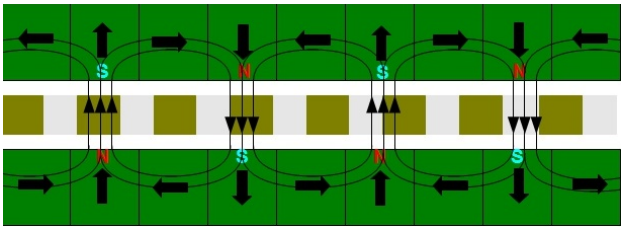

Fig. 8: Halbacharray with 90° shifted magnets

density than with 90° shift. It is possible to achieve $0.6T$ air-gap flux density with this topology, which is enough to design a high performance machine [10]. The main advantage with Halbach array is to remove back iron, resulting in a lighter machine with very high efficiency[11].

Stator assembly options

The stator can be iron-free or contain magnetic iron. The iron-free stator disc is manufactured by placing the stator coils in a mold to be filled with epoxy. In bigger machines with large mechanical forces, the epoxy may be supported by carbon fiber. When having iron present in the stator, it can be a slotted or non-slotted stator. The non-slotted stator is very simple, where stator coils are glued to an iron disc as seen in Fig. 1. The stator shape has an impact on the cogging torque from (5). Since the rotor magnets and copper have the same permeability as air, a machine with non-slotted stator will have no variation in magnetic reluctance when rotating, hence no cogging torque.

The slotted stator iron provides a more solid structure. Using the stator slots to house the stator coils will prevent any movement. The air-gap magnetic field will go through the iron teeth instead of the coil, and because of this the conductor size may be higher due to lower eddy current losses. The disadvantage is that the introduction of slotted stator will generate variable air-gap reluctance, resulting in high cogging that will leave the machine unusable if not taken into account in the design process.

Fig. 9: Patented coil geometry

IV. Description of patent

The coil design to be investigated in this report is patented by J.E. Brennwall [12]. The scope of the patent is a coil assembly for a three phase brushless PM axial flux multidisc machine, where the coils have machined cuts to create a flat coil arrangement. The purpose of a flat coil arrangement is to allow a compact multidisc arrangement, allow high cooling capability, and an easy assembly method. In Fig. 9, the coil design is presented.

A design goal is to maximize the fill factor of the machine. To do this, the coils needs to be overlapping; the area within a coil is filled with conductors from neighboring coils. This is usually done by bending the end-winding axially. The advantage of having the coil cuts is that the airgap area can be filled with conductors while the end coil and the active stator part have equal axial thickness, which in other designs are only possible if using concentrated non overlapping windings. An example of this is shown in Fig. 10 and Fig. 11.

An advantage of this design is the large surface between cooling medium in the air-gap and the stator, and that the cooling medium is in direct contact to all conductors. This

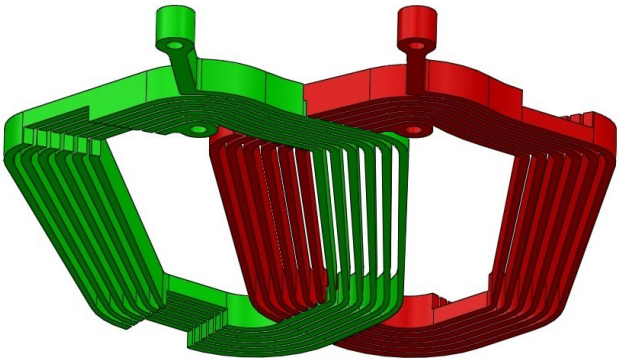

Fig. 10: Coil assembly

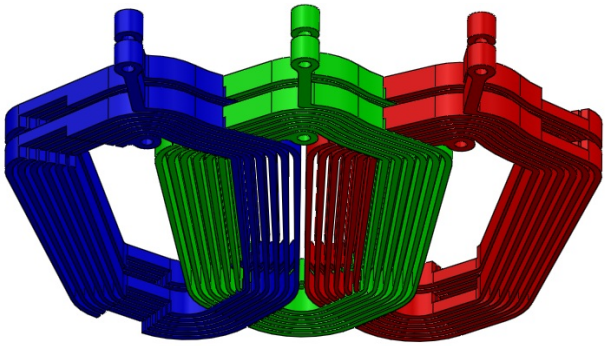

Fig. 11: 2 layer, 3 phase assembly

Fig. 12: 3-layer, dual leveled, lap windinded, slotted internal stator AFPM,

allows a very high current density and a compact machine design.

In an axial flux machine, the limiting width of the conductor is at the inner radius. Since the pole pitch is increasing with the radius, more space is available for the conductor at the outer diameter. By using water-cutter to produce the coil, a variable conductor thickness may be used. The increasing pole pitch can be compensated with wider conductors, resulting in a very high fill factor.

An example of an axial flux machine design with the coil design, is presented in Fig. 12, 13, and 14. The internal stator coil has been separated into three coil layers as seen in Fig. 14, due to better cooling and lower phase current. In the coil design, every other turn has been removed and inserted with laminated magnetic iron, stretching through all coil layers in order to lower the amount of magnets used in the machine. The important aspect of this design is the ability to cool the internal stators, which gives access to high current densities. This design has an outer diameter of $2.1m$, current density of $10A/mm^2$, average torque production of $157kNm$, an efficiency of 88% at 150 rpm, $124kNm/m^3$ torque density, and uses $300kg$ of PM material.

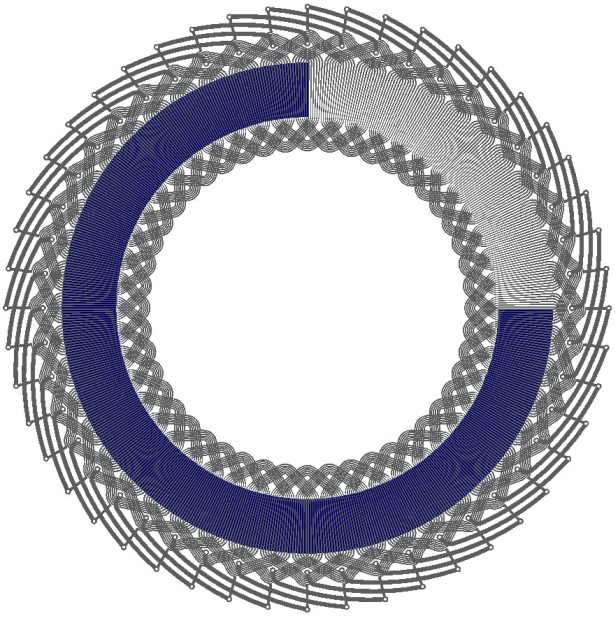

Fig. 13: Stator layout

V. Wire conductor versus solid conductor

The main feature of this design is the ability to transport heat out of the machine. A very important observation is that copper wires are usually insulated with a material with very

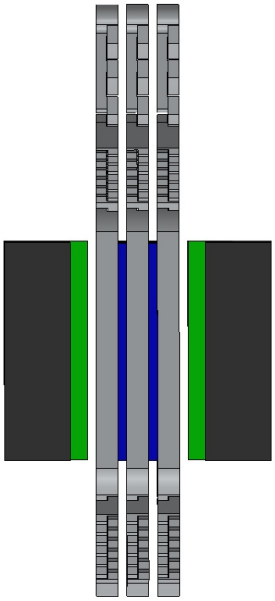

Fig. 14: Side view sheet

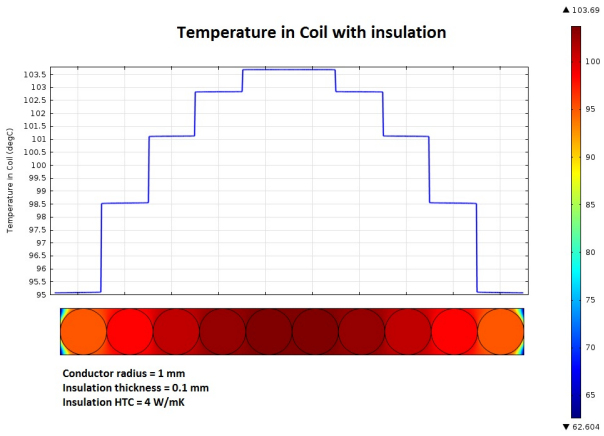

Fig. 15: Temperature in coil, with wire insulation

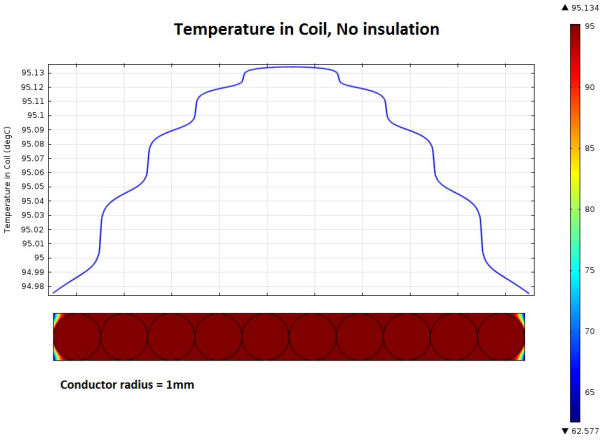

Fig. 16: Temperature in coil, without wire insulation

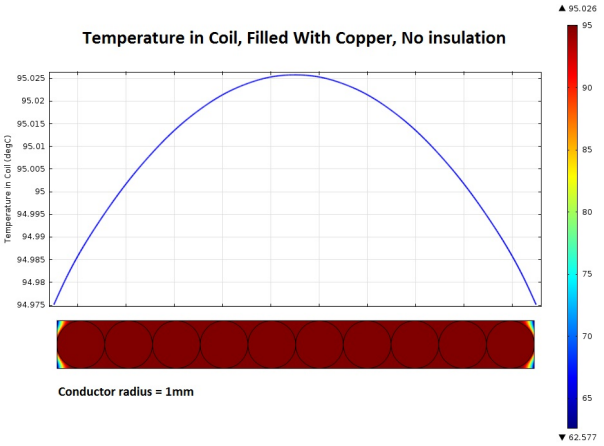

Fig. 17: Temperature in coil, with solid conductor

low thermal conductivity, while copper itself is highly thermal conductive. When using copper wires to wind a coil, the heat generated inside the coil has to be transported out by flowing from one wire to the next. Each time it needs to overcome the thermal resistance of the insulation, a temperature difference is needed, and results in a higher temperature inside the coil than on the outside. In Fig. 15 a COMSOL simulation is done to visualize this phenomena. The model consists of one layer with winded copper wires. The box around the copper wires is air, with ”periodic condition” on the upper and lower boundary, and ”heat flux” for cooling on the left and right boundary. The heat generation is modeled as a heat source on all copper wires, and the insulation is modeled as ”thin thermally resistive layer” boundary. The typical thermal conductivity for the insulation is $4W/mK$, and is modeled as $0.1mm$ thick. The figure shows that the thermal barrier in the insulation is preventing the heat flux to exit. With the ambient temperature set by COMSOL, the temperature difference between the outer- and the inner-wire is $8.7°$, which will increase proportional with increased power dissipation. This becomes a problem in high current densities, where the high level of power dissipation gives a very high temperature difference between the internal and outer part of the coil.

To show the difference with and without thermal insulation on the copper wires, another simulation is done by disable the ”thin thermally resistive layer” boundary condition in Fig. 16. The temperature gradient between inner and outer wire is now dictated by the thermal resistance in the copper itself, along with the thermal connection between the wires. The temperature difference is now only $0.144°$. However, to remove the insulation on the copper wires is not practically, because it is now short circuited. The coil design presented in this paper uses solid wire instead of multiple turns to achieve the low temperature gradient as seen in Fig 16. To simulate

this, the air between each round copper wire is replaced with solid copper, resulting in one solid wire. The same power dissipation is used as before, and the result can be seen in Fig. 17. Now the temperature is a continuously changing curve, with only the thermal conductivity of copper to dictate its shape. The temperature difference is $0.05°$, which is very low. The temperature inside the coil can easily be controlled by measuring the temperature on its outer surface, and having such control decreases the safety factors and increases the amount of current that can be supplied to the machine.

The AC-losses increase when having solid conductors because of the high cross-section, and due to this the machine must operate at low frequencies. The solid conductor increases the fill factor of the machine, and gives better cooling capability. Because of this, the coil design is suitable for low-speed high-torque applications.

VI. Coil design - active part

The active part of the stator is the area which interacts with the rotor PMs, an example of this can be seen in Fig. 14. It can be designed to contain iron or not, having an impact on the optimal axial stator depth, and the amount of PM material used in the machine. A circumferential 2D sheet of the machine design is shown in Fig. 18 and 19, where the design is containing iron and no iron respectively. In both designs, active cooling medium is removing heat from the conductors in the air-gap and in the internal cooling ducts, having a very high capability of removing heat. When dividing one coil layer into two layers and introducing a cooling channel in between, the fill-factor will go down, but the cooling surface area has doubled for the same machine, and it can carry 25% more current. The torque is increasing proportionally with the current, but the resistive losses are proportional to the current squared, resulting in a low efficient but high torque density machine.

For an iron free stator, the PMs need to overcome both the airgap and the axial depth of the machine. To be able to have a sufficient magnetic field strength and a low-cost machine, it is preferable to introduce iron in the stator as seen in Fig. 19. The iron reduces the fill-factor of the stator, but allows a much longer axial depth. The amount of iron compared to conductors in the stator cross-section is determined by optimization between magnetic and electrical loading, along with optimal axial depth. Introducing iron in the stator design comes with difficult challenges, like cogging torque and highly distorted back-EMF waveform, which will be discussed later in detail.

VII. End-turn reduction

The purpose of the stator end winding is to couple together the conductors in the active coil part into a system of a certain amount of phases and stator poles. The end coil is conducting the stator current and contributes to the total power loss in the machine, but since it is not situated in the magnetic field from the rotor it does not contribute to the main torque production. To minimize the amount of end coil

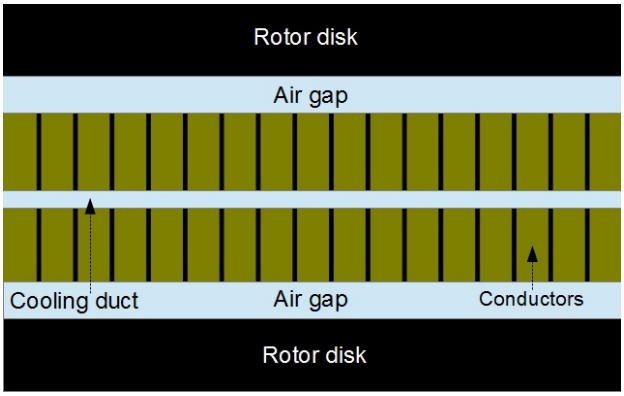

Fig. 18: 2D sheet of active part in stator, iron free

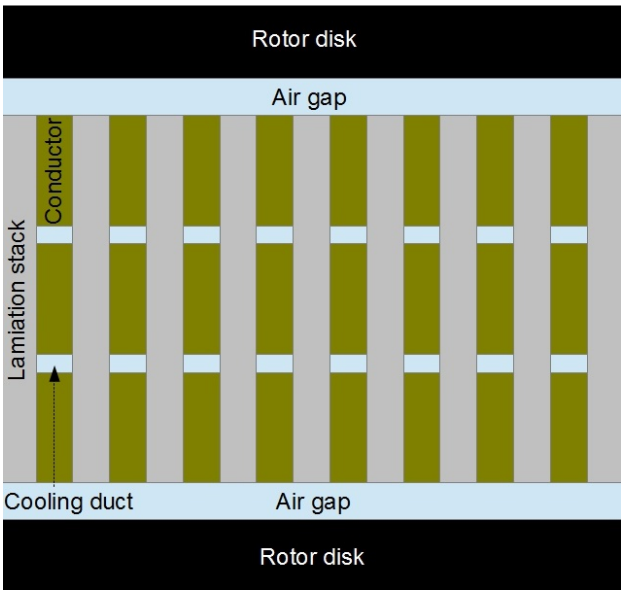

Fig. 19: 2D sheet of active part in stator with laminations

is therefore a very important aspect of machine design. One of the disadvantages of the axial flux machines compared to its radial counterpart is the amount of end coil compared to the active stator part, and often more than half of the total copper in the machine is situated in the end winding. How the stator active part is connected together is also important to the back-EMF waveform. Various techniques are used to shape its waveform using end-winding coupling, and some of these techniques also reduce the amount of end-coil volume. The most used method is reduced pitching or fractional slotting - implying that the return path of the coil is less than the pole pitch, which reduces the maximum torque but significantly reduces the end winding volume and at the same time provide a lower harmonic content in the back-EMF. However, the methods requires a two layer winding, and is not applicable in this design, due to the manufacturing method and the use of internal cooling ducts. Because of this, the end coil has a given minimum length it must travel based on the number of poles and phases in the machine.

There are two winding topologies, lap- and wave-winding, which can be applied to this machine, being freely to choose the number of phases and poles in the machine, gives some room for experimental design to reduce the end coil volume. The following examples in this text have not been optimized, but for visualization purposes only. The same active coil region is used in all examples, having an outer diameter of $1.8m$ and inner diameter of $1.4m$. If the machine is required to use a three phase system, the end coil design needs to be in a triangular shape to be able to maintain its flat configuration as shown in Fig. 14. This is because it needs one cut on each side of the end winding, meaning that a certain distance is needed between the cuts for the current to cross, visualized in Fig. 20.

Wave-winded parallel connected turns: The minimum end coil volume with the triangular shape is with a continuous wave-winded coil with parallel connected turns, and will function as a base design to compare with the following end coil designs. An example of this is shown in Fig. 21. The end coil volume of this design is 50%, but can be improved by changing the K_D of the machine. The advantage of a wave-winding is that the entire phase coil, or segments of it, can be manufactured as one piece, eliminating the need for connectors between each phase coil like the design in Fig. 23. Due to parallel connected turns, the effective coil cross-section will be very large, and contributes to large circulating eddy currents.

Wave-winded series connected turns: To connect the phase turns in parallel increases the circulating eddy currents within the phase. To avoid this, the turns are connected in series, but require more end coil volume. An example of a series connected wave-winding is shown in Fig. 22. In this design, the different wave winding segments are connected together after two ”waves”, and at these connections a large contact surface is needed to provide a low resistance. The end coil volume of this design is 57.5%, 7.5% more than the minimum topology.

Lap-winded series connected turns: The most usual topology is the lap-winded three phase design. An example is shown in Fig. 23. A coil is called a lap-winding when it is winded around the same point for all its turns. Because of this, it needs to be connected to the next coil in the same phase by a connector. The end coil volume of this design is 60%, 10% more than the minimum topology. This increase is mainly because of the need for connectors which is not needed in the wave-winding design. Due to connectors and the goal of having a flat coil configuration, another cut in the coil is needed as well as a higher connector point, as shown in Fig. 24. This increases the resistance and adds more complexity to manufacturing and insulation.

Lap-winded unbifurcated series connected turns: All the examples till now have been for a 32 pole machine. To design a winding with fewer poles, each phase coil has to connect to the

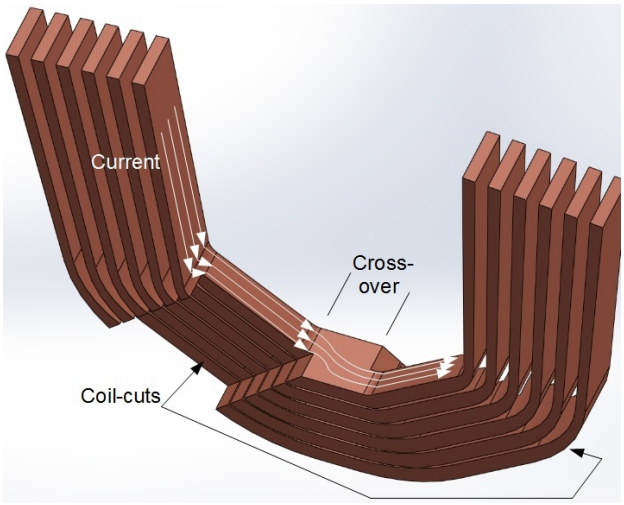

Fig. 20: End coil cuts on opposite sides in 3 phase topologies demand a cross over area

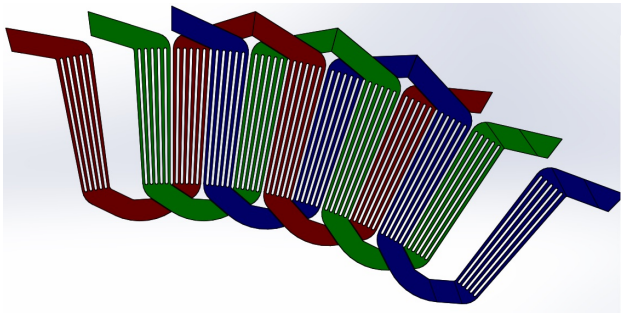

Fig. 21: 3 phase, 6 turn, 32 pole, wave-winded end coil topology

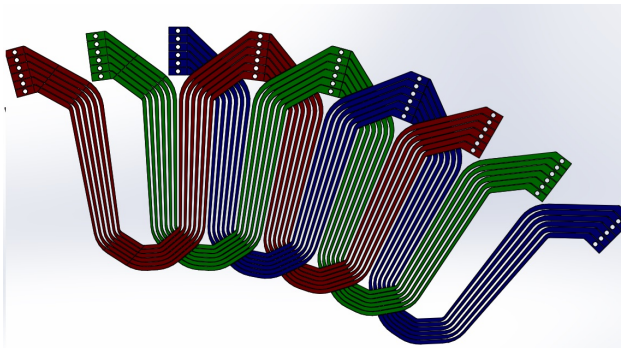

Fig. 22: 3 phase, 6 turn, 32 pole, wave-winded end coil topology

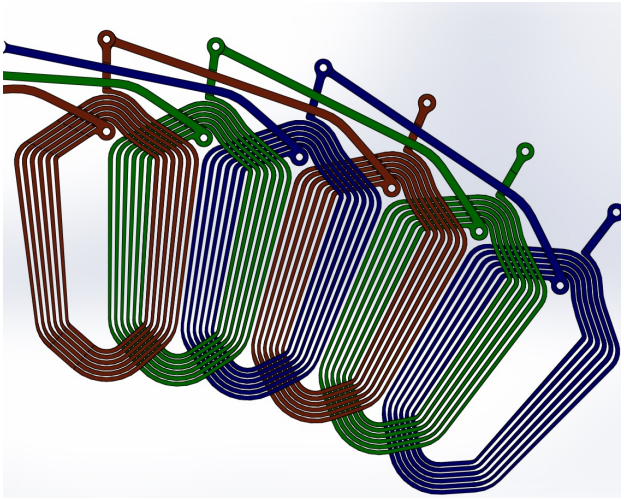

Fig. 23: 3 phase, 6 turn, 32 pole, lap-winded end coil topology

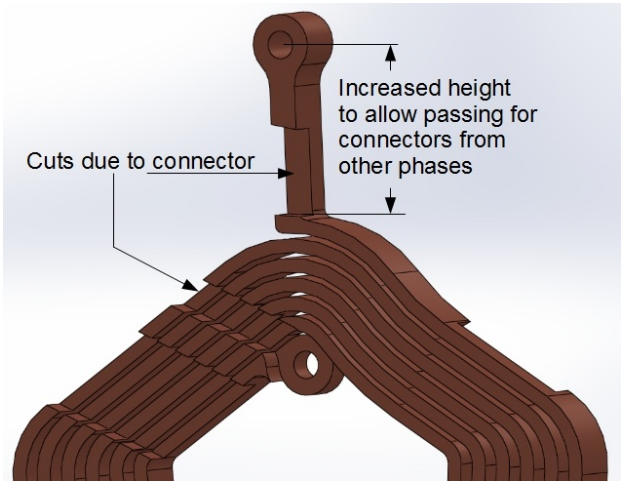

Fig. 24: Coil cuts due to connectors between phase coils

active coil part over a larger span. When lowering the number of poles for a given machine diameter, the end coil has to travel a longer circumferential length to connect to the return path of its slots. At low polenumbers it is preferable to divide the slots dedicated to one phase in a pole span into two separate coils. The two coils are not co-centric and spans different directions, hence called a unbiforcated coil. The two coils will have a lower end coil volume, compared to the single coil. This can be done for both wave- and lap-winding topologies, an example of this design is shown in Fig. 25. The disadvantage of having two coils instead of one is that another two cuts are needed in the phase coil. To assemble this design, two different versions of the coil are needed, where the connector goes right or left to connect the phase coils in the correct manner (this is not shown in the figure). The end coil volume of this design is 65%, which is not that much higher than the previous designs. Considering that the pole number is half, the rotational speed is doubled at the same electrical frequency. The power output is twice the original 32-pole machine with the same amount

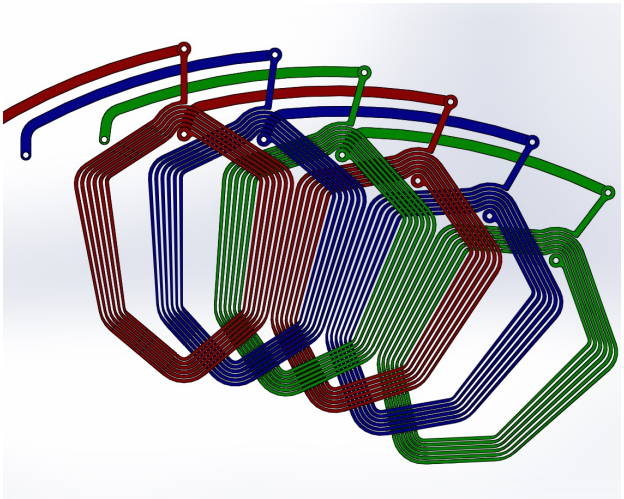

Fig. 25: 3 phase, 12 turn, 16 pole, lap-winded end coil topology

of DC and half the AC losses, which again provides a higher efficiency.

VIII. Material Choices and Manufacturing Possibilities for the Stator

The patented stator design enables a cheap production and simple assembly. The preferred production method is to use either water-cutting or molding. The focus has been to have the same design in each coil in each phase, so that in a production situation there exists only one part which is mass-produced.

Water-cutter: When using a water-cutter to produce a coil, the entire geometry including connectors may be produced, using a 5-axis water-cutter[16]. However, the traditional water-cutter only cuts in one direction, meaning that the coil cuts shown in Fig. 20 must be made before or after the water-cutting, resulting in a two-step process to produce the finished coil. When using lap-winded coils, the connector needs to be separately produced, and be connected in the assembly process. In the case of a wave-winded coil, the entire coil or segments of it may be produced in a single process -meaning less individual parts and faster production and assembly. But for bigger machines it is not applicable to make the entire coil on one part, because of the weight and the possibility to assemble the stator in segments before constructing the machine on site. The advantage of a water-cutter is that it can cut out a geometry with a precision of $0.02mm$, and the plate can be up to $25cm$ of stainless steel[16]. However, a thick plate will require longer cutting time and lower accuracy.

Molding: Another method to mass-produce the coil parts is to use molding. The molding process is much faster than the water-cutting, and no spear metal will be lost in this process. Two iron molds are produced to make one specific coil type. The two molds will be filled with melted aluminum or copper, and in matter of seconds the melted metal is cold enough to be taken out. The advantage of this production method is that it is the capability of producing many coils simultaneously

by having multiple iron molds, it has high start-up costs but low production cost. The disadvantage of using molding is the geometric limitation to detail and thickness. The mold needs a certain slip-angle of $1.5 - 2^\circ$ and a minimum detail thickness (conductor width) of $4mm$ [17].

Stator Laminations: Due to reduction in PM material costs, the use of iron in the stator is presented. The magnetic iron is to be placed in the active coil area between each conductor turn. The iron needs to be laminated since it is situated in the air-gap magnetic field. In the coil design, the conductors leave a constant gap between them through the active part of the coil. The reason to have a constant gap is to make the production of laminations much easier. The shape of the laminated iron is rectangular with parallel sides - meaning that the production of the lamination can be done by cutting the same sized lamination. After that, stacked together to fit between the conductors. The conductors in the stator are not to be insulated, and because of this the lamination-stack has to be coated with insulation. The insulation may be enough to hold them together until assembled in the machine, but if not, each lamination plate has to be glued to the next, reducing amount of iron to be fitted in the stator. The lamination must be pressed-fitted into its slots, so there is no room for movement. Due to many laminations facing the magnet, the attractive force per lamination is not that high. A quick calculation of the attractive force can be done by

$$F = \frac{\delta W}{\delta x} = \frac{\delta}{\delta x}\left(\frac{1}{2}\int_V H \cdot B dV\right) = \frac{B_g^2}{2\mu_0}A \qquad (6)$$

where B_g is the air-gap flux density and A is the surface area of the iron facing the air-gap. Quick calculation on the design in Fig. 12 shows that each lamination stack feels an attractive force of $257.83N$. However, as long as the lamination is centered between the rotor discs, the forces cancel each other out.

The magnetic field conducted by the lamination is in general only in the axial direction. Therefore, standard transformer lamination of $0.35mm$ or $0.5mm$ thickness can be used. The material cost of the lamination is very low, and the production of the lamination stacks can easily be automated. However, the assembly of the lamination in the stator, with multiple stator discs with a certain distance is required between each disc, is a problematic process which is not solved yet.

IX. Copper versus aluminum conductor

Copper is commonly used as conductor material in electrical machines due to its excellent conductive property. However, the price of copper has been increasing over the last decade, and is now considered a very costly metal. As a response to this, aluminum has been introduced into a number of applications to replace copper. Aluminum is a cheap, light-weight metal, with about 60% conductivity of copper. The material properties of copper and aluminum is shown in table I.

Compared to copper, the aluminum oxidizes instantly in contact with oxygen. The oxidation layer is highly resistive, and is problematic when connecting aluminum coils together. The contact surface needs to be larger with aluminum coils compared to copper coils. This present a problem when having many connections and restricted space in the stator.

The natural oxidation of aluminum provides a protecting and electrically isolating surface. To increase the oxidation layer the aluminum part can be anodized, resulting in higher electrical insulation and more protective against external damages. Copper oxidizes slowly, and it is not difficult to remove any oxidation to achieve a good contact surface. However, the copper needs to be coated with an insulator. The insulation is very thick and has a low heat transfer capability compared to the oxidation layer of aluminum.

If copper is used in the machine, the surface facing the cooling liquid will not be insulated, provided that the cooling mediums dielectric strength is suited to the voltage level. Without insulation on the copper, the heat transfer will be larger than from aluminum, together with higher thermal and electrical conductivity. But due to higher cost and weight, copper is more suited in high performance machines.

X. Cooling of Stator

Cooling mediums considered in this design are water and air. Transformer oil or other such liquids can also be used, but is not considered here. The axial flux machine acts as a natural centrifugal pump when rotating, where it pushes air or water radially out from its center. If the operation of the machine provides sufficient flow, there is no need for any external fan or pump. The centrifugal effect is enhanced by salient features in the rotor design. In Fig. 12 this is done by designing the rotor as a wheel with spokes together with salient magnets.

The key parameter that influences the cooling capability is the HTC - Heat Transfer Coefficient. The HTC has units Watts per Kelvin per surface area, and determines how much energy the cooling medium can extract per second from the stator coil. The HTC is proportional to the temperature gradient between the cooling medium and heat source, and proportional to the surface area between them. The HTC is heavily influenced by the flow and phase of the cooling medium. For example, at low speeds, the medium will have a laminar flow with a thin film close to the stator surface. This will act as a boundary layer and not mixed with the rest of the flow. The medium within this boundary will be heated, and soon reach a higher temperature than the surrounding flow. With a lower temperature gradient between the coil and cooling medium will proportionally reduce the amount of energy removed from the coil. At high speeds the flow is turbulent, and heated medium at the heat source will quickly be removed and replaced with colder medium, keeping the entire flow heated. Hence, the temperature gradient will be higher and extract more energy.

Obviously, it is a goal to ensure turbulent flow. The turbulence is dependent on the speed of the medium and its flow inside the machine. By introducing salient features or rough surfaces, the turbulent flow will occur at lower speeds and ensures sufficient cooling. To maximize the surface area between the cooling medium and heat source is another way

TABLE I:
Difference between aluminum and copper [18][19][20][21]

Parameter	Aluminum	Copper	Difference Al to Cu
Electric conductivity, σ	$3.5e7S/m$	$5.96e7S/m$	58.7%
Temperature coefficient	$0.0039K^{-1}$	$0.0039K^{-1}$	0%
Specific weight, ρ	$2700kg/m^3$	$8020kg/m^3$	33.6%
Thermal conductivity, U	$237W/Km$	$401W/Km$	59.1%
Insulation thickness/aluminum oxide, δ	$50-100nm$	$0.01mm$	1%
Insulation thermal conductivity, U_{iso}	$40-50W/Km$	$3-4W/Km$	1000%
Price per kg	$11.2NOK/kg$	$42NOK/kg$	72%

TABLE II:
HTC to metal with forced convection[23]

Cooling medium	HTC
Air	$10-100W/m^2K$
Water	$500-10000W/m^2K$
Boiling Water	$3000-100000W/m^2K$

to ensure sufficient cooling. The coil is designed to separate each turn from each other, and since the machine is to be filled with water, the entire coil is in direct contact with the cooling medium.

The HTC is a highly geometric and flow dependent variable, and no exact approximation can be used. The HTC of forced convection between air, water or boiling water to metal is shown in table II. The water is clearly more efficient than air, but using water as a cooling medium is complicated and increases manufacturing and operational costs. By designing the machine to tolerate high temperature and pressure, the cooling strategy can allow the water to boil on the conductors. The capability to remove heat from the machine in this case is extremely high, and very compact machines can be constructed due to this. However, the magnets in the machine are sensitive to temperature, weakened by increasing temperature, and may be demagnetized if not designed correctly.

In the case of using air as a cooling medium, the outer housing may have vents to ensure sufficient flow. Using water, the task is more difficult. The outer housing must be water tight, and the inflow and outflow of water must be designed correctly to ensure evenly distributed cooling in the entire machine. The analysis of the flow and HTC may be done using FEM-tools, but it is a three dimensional problem, and with turbulent flow the simulation time is long and may not converge. The best way to analyze the flow and HTC is to make use of a prototype and compare the results to the simulation, hence altering the simulation to converge with lab-results. A small scale prototype is suggested and has been manufactured. The prototype is shown in Fig. 26. The main purpose of this prototype is to estimate the HTC between water and aluminum at laminar and turbulent flow for different air-gap lengths. The geometry of the coil in the prototype is to recreate the active stator part with solid conductors and laminated magnetic steel, giving an indication of the HTC of a full size machine. The testing and results from this test is covered in the master thesis of the student Lars Clad from the department of process and engineering [1].

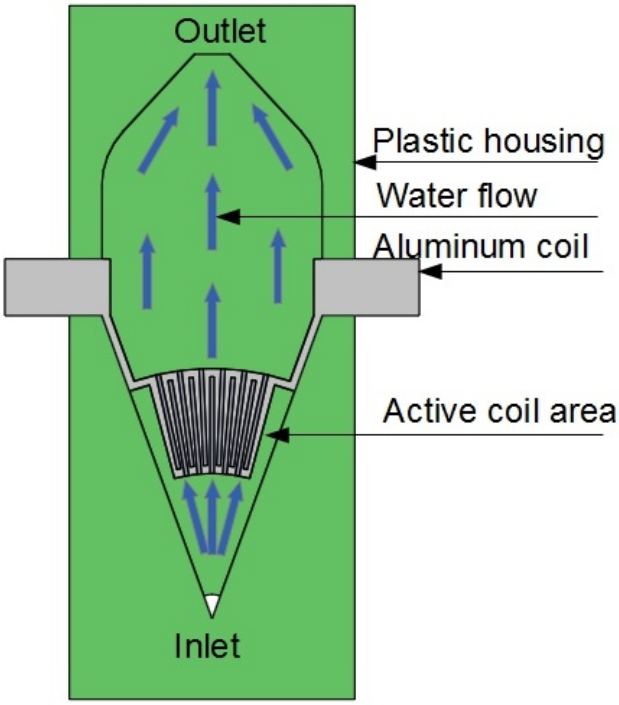

Fig. 26: Prototype designed for laboratory testing of HTC and water flow

XI. Back-EMF waveform

The back EMF voltage is the induced voltage appearing in the stator conductors, due to the rotational magnetic field from the rotor. From (1) the force acting on a charge q due to time varying magnetic field is given. The electric field strength $\vec{E}$ is defined as

$$\vec{E} = \frac{\vec{F}}{q} \tag{7}$$

Combining with (1), the voltage is defined by the magnetic field as

$$\vec{E} = \vec{v} \times \vec{B} \tag{8}$$

The voltage e is defined as

$$e = \int_l \vec{E} \cdot \vec{dl} = vBl \tag{9}$$

where B is the external magnetic flux density waveform, l is the length of the conductor and v is the rotational speed of the magnet. The induced voltage is proportional to the rotational speed of the machine, air-gap flux density and the active length of the conductor. An important observation here is that when the rotational speed is constant, the back-EMF waveform is equal to the waveform of the air-gap magnetic field. The induced voltage in one slot in a machine is given by equation (9), the induced voltage in the next slot will be the same but phase shifted due to the distance between them. When several slots are connected in series by the end coil arrangement, the induced voltage of each slot is simply added together, keeping in mind their respective phase shift. The resulting voltage waveform is called the back-EMF, and as it is proportional to the rotational speed it is often called speed voltage.

The back-EMF voltage is the terminal line-ground voltage of a Y-connected generator at no-load (open terminals) condition. For a motor the back-EMF will act as a voltage drop in the phase winding, where the terminal line-ground voltage is the sum of the back-EMF and voltage drop over the phase resistance and leakage flux. When the terminal voltage is higher, the speed of the motor will increase until the back-EMF neutralizes the voltage difference. Hence, for a given maximum voltage of a converter or grid connected to the motor, the back-EMF will determine its maximum speed.

The back-EMF in a conductor with PM excitation is square-waved and can be decomposed into a harmonic distribution of sinusoidal waves as seen in Fig. 27. The same harmonic distribution is present in the back-EMF voltage. The instantaneous power is defined as current times voltage, the energy or work produced by the power is the integral of power over time:

$$W = \int_0^t e(t)i(t)dt = \sum_{i=1}^{\infty} \int_0^t \hat{e}_i sin(i\theta)\hat{I}sin(\theta)dt \qquad (10)$$

In Fig. 28 the harmonic content of the back-EMF together with the applied phase current are plotted. For all θ, the current and fundamental back-EMF component has equal sign, meaning that the power $p_1 = e_1(t)i(t)$ is always positive. The third harmonic of the back-EMF is alternating between positive and negative value while the current is positive, and taking the integral of its instantaneous power, it adds up to zero. The same is true for the fifth harmonic and the rest of the harmonic content. The energy provided by the back-EMF and current is reduced from (10) to:

$$W = \int_0^t e(t)i(t)dt = \int_0^t \hat{e}_1 sin(\theta)\hat{I}sin(\theta)dt \qquad (11)$$

This means that only the fundamental voltage of the back-EMF waveform is producing real power. The rest of the harmonic content is producing an average of zero energy, where it is producing energy in one instant and consumes energy in the next, also known as reactive power. The reactive power is contributing to the total current, and hence the total power loss, in the stator.

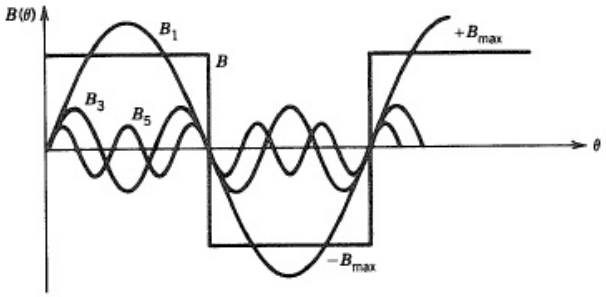

Fig. 27: The harmonic content of a square-waved air-gap magnetic flux density [13]

Only the fundamental component of the back-EMF can be used to produce or deliver power to the machine, therefore it is very important to minimize the harmonic content of the back-EMF waveform and maximizing the fundamental component. This is especially important in grid-connected machines, where the harmonic content must be drawn from the grid itself, contributing to high reactive power loss in the transmission grid. To do this, the phase back-EMF waveform needs to be as close to sinusoidal as possible. The machine design can only have integral slotting, and there are two possible methods to shape the back-EMF. The first is to use distributed windings, which means that the turns in a phase coil is placed in different slots in the stator where the spacing between them contributes to a more stepwise change in the back-EMF waveform. The other method is to change the span or shape of the magnets. To shape the magnets is to have a variable axial length from small to large to small, so that the resulting air-gap flux wave-from is sinusoidal. This is often done with salient rotor poles in bigger machines with field windings and laminated rotor core. The effect from shaping the magnets will not be included in this paper.

The two methods which influence the back-EMF waveform are expressed as the magnet span $\alpha_m = \tau_m/\tau_p$, and the number of slots per pole per phase q. The shift in electrical degrees for each slot can be expressed by q and number of phases ph as

$$\theta_{shift} = \frac{180^\circ}{ph\ q} \qquad (12)$$

A simple model has been made to investigate the influence of q and α_m on the harmonic content. A perfect square-waved air-gap flux density is used to model the back-EMF waveform, and a Fourier analysis in Matlab provides the intensity of each harmonic. The step size used for α_m is too small to give exact results, but the purpose of the model is to find the tendency of their influence on the harmonic content. To compare the results from each q and α_m, the total harmonic distortion (THD) is used. The THD is defined as

$$THD = \left(\sqrt{\sum_{h=2}^{\infty} \hat{e}_h^2} \right) / \hat{e}_1 \qquad (13)$$

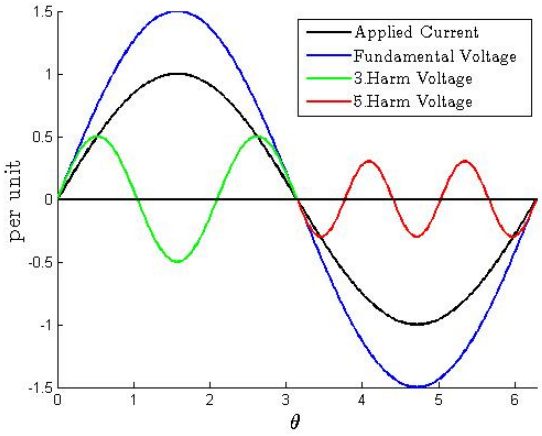

Fig. 28: 1., 2., and 3. harmonic of back-EMF voltage with stator applied current

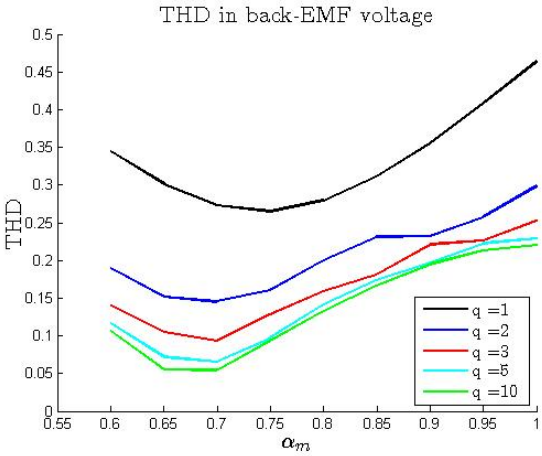

Fig. 29: THD form different q, swept from $\alpha_m = 0.6$ to 1

The results from varying the magnet span and number of turns are show in Fig. 29. The THD has an optimal minimum for each q. The tendency is that the THD is reduced when increasing q, and its minimum point is moving toward a lower α_m with increasing q. For high q, the magnet pitch should be in the range of $0.65 - 0.7$ to achieve minimum THD. To calculate losses due to the harmonics, super-position can be used to find the current contribution from each harmonic order - keeping in mind that the inductances are increasing with frequency and therefore lower the influence from the higher harmonics.

In electrical machines, the use of distributed windings and fractional pitching reduce most of the high harmonic content in the back-EMF. However, the lower harmonics from third to eleventh can still contribute to a high THD. By using a three-phase winding and star connected termination internally in the stator, some of the harmonics cancel out due to the $120°$ shift between the phases. The criteria for which harmonic to be canceled is determined in relation to its waveform. If it has an integer number of periods within $120°$, the harmonic

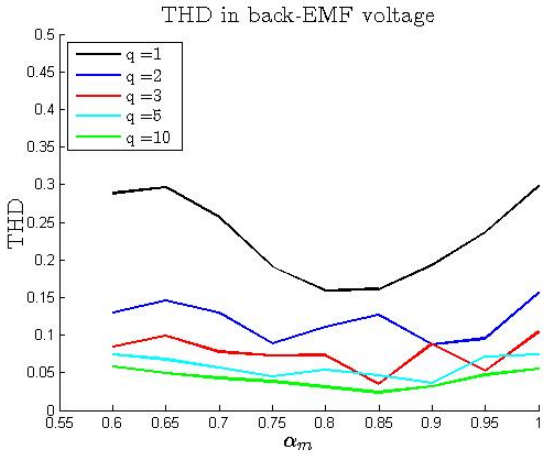

Fig. 30: THD form different q, swept from $\alpha_m = 0.6$ to 1., 3., 9., and 15. harmonic canceled

is canceled, and can be found using the relation

$$\frac{120h}{180} = \frac{2h}{3} = (integer) \tag{14}$$

where h is the harmonic number. Of the low harmonics it is found from (14) that the $3rd$, $9th$ and $15th$ harmonic is canceled, and another THD plot is generated assuming a 3-phase star connection in Fig. 30. In this figure, the minimum point of THD is still reduced when increasing q, but the tendency is that the minimum point moves toward high α_m, suggesting a α_m between 0.8 to 0.9 when q is high, which is a different conclusion compared to the results in Fig. 29.

After the removal of the lower harmonics with three-phase star connection, the remaining contributors to THD are the $5th$, $7th$, $11th$ and $13th$ harmonic. For a given q and swept over α_m, each harmonic varies between a high and low peak with a certain period. This can be seen in Fig. 31. The step size of α_m is too small to correctly show the variation, but it can be seen that when the $5th$ and $7th$ harmonic is at their minimum, the $11th$ and $13th$ harmonic is peaking, and vice versa. Because of this it is difficult to completely eliminate all harmonics, but the minimum point in Fig. 30 can be used as a reference to minimize their influence.

Due to the possibility of a high number of distributed slots in the design presented in this paper, the resulting THD in the back EMF can be very low. For a stator with 3 phases, 16 poles, $q = 12$ and $\alpha_m = 0.85$, shown in Fig. 12, the THD will have a value of less than 2.5% which is very low. In addition, the methods of reducing cogging as presented in the next section give smoother transition between each step in the back-EMF waveform, contributing to an even lower THD. The drawback of having a high q is a higher winding factor, which reduces the amount of torque produced.

XII. Cogging torque reduction

When slotted iron is present in the stator, the magnetic reluctance seen by the magnets is changing as it is rotating.

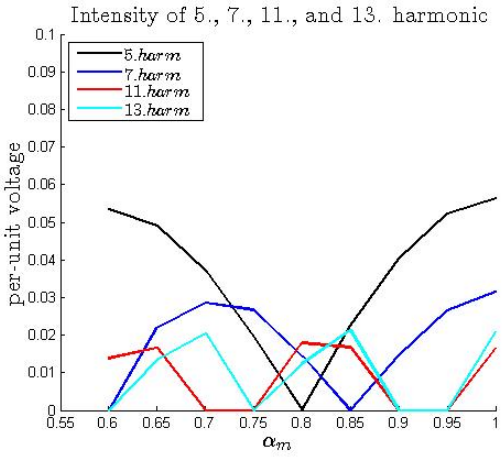

Fig. 31: Intensity variation in 5., 7., 11., and 13. harmonic swept from $\alpha_m = 0.6$ to 1

The magnets want to position the rotor so that the flux-linkage is at its maximum. When the rotor is offset from this position, a circumferential attractive force is generated attempting to align the magnet and the stator iron teeth to achieve minimum reluctance and maximum flux linkage. This contributes to a near sinusoidal ripple on the output torque. The harmonic frequency of this ripple is dependent on the number of iron teeth in the stator. Its mechanical frequency is given as

$$f_{cogging} = \frac{p}{2} \cdot q \cdot ph \cdot rps \tag{15}$$

where rps is the rotor rotation per second.

The torque ripple is zero at detent positions, because this is where the flux linkage is either at maximum or minimum. A stable detent position occurs when the flux linkage is at its maximum, and the attractive force will try to position the magnets and stator teeth to this position. This is the practical feeling with cogging, where the rotor wants to "jump" between each stable detent position when it is rotated. During operation, the cogging will generate noise, vibrations and ripple in the torque output of the machine. If no effort is done in minimizing the cogging, the result can be that the machine is unusable. This topic is well described in literature [2][14][15]. The magnitude of the cogging force between rotor magnets and stator slots from (5) is

$$T_{cog} = -\frac{1}{2}\phi_g^2 \frac{dR}{d\theta} \tag{16}$$

where ϕ_g is the air-gap flux due to the rotor magnets and R is the magnetic reluctance seen by the magnet. To minimize the cogging torque, the change in R or the magnitude of ϕ_g must be reduced. Another method is to change the shape or the position of the magnets in the motor so that the cogging from one magnet is canceled by another. The different methods to reduce the cogging effect also smooth the back-EMF waveform and reduce THD - the design process should take both into account when optimizing. The alternation of magnets to reduce the cogging will also reduce the output torque in some degree. This will be discussed more clearly in the analytical model section. Some specific methods to reduce cogging torque, and how applicable it is to the machine design, are presented in the following text.

Magnetic Wedges: Due to slotted stator, the magnetic reluctance vary with position. By introducing a magnetic material to close the slot opening, it reduces the variation. In [15] this is done to a machine with $q = 1$, resulting in a reduction of 40%. Using wedges to close the slot openings will prevent the cooling medium to have direct contact with the conductors, and reducing the cooling capability in the active area.

Reducing Air-gap Flux: From (16) the cogging is proportional to the squared of the air-gap flux, while the electromagnetic torque is proportional to the air-gap flux. Therefore, a small change in ϕ_g will reduce the cogging while the produced torque is not that affected. To lower the air-gap flux, the magnet remanence or the magnet length is lowered. According to [14] this technique is the most effective method to reduce cogging, but because it reduces the performance of the machine it must be optimized along with other techniques presented here.

Changing Magnet Shape: When the magnet is shaped so that the end boundary is parallel to the slot, the entire length of the magnet will produce the equal cogging force. Because of this, the cogging will be very high. An alternative is to skew the magnet to not be parallel to the slot. In that way the peak cogging force will appear at different times along the boundary of the magnet, resulting in a lower total cogging force. An example of this is shown in Fig. 32. Due to the skewing, the magnetic flux density is lowered. The skewing gives a smoother step in the back-EMF waveform reducing its THD. In the machine design presented in this report, the q is really high, and because of that the amount of skewing needed is very low, resulting in very little influence in the overall performance. Since the direction of the attractive force is changing when passing a detent position, the magnet can be skewed so that the upper and lower corner spans over two detent positions. In that way the upper half and the lower half of the magnet boundary produces equal but opposite directed cogging force, and the resulting cogging torque equals to zero.

Varying Magnet position: The latter techniques presented are focusing on the cogging reduction from one magnet alone. Another approach is to look at the cogging force acting on all rotor poles. If the rotor poles are symmetrically placed around the rotor, any cogging force experienced from one magnet will be equal to the cogging force in all rotor magnets. If there is any cogging present at one magnet, the resulting cogging of the machine will be very high. By placing the magnets unsymmetrically around the rotor, their peak cogging force will occur at different positions. To create an unsymmetrical rotor, every other magnet on a symmetrical rotor is shifted in one direction. As a result, the total cogging will be decreased. Since the q in the machine design in this report is very high, the shift in magnets can be so that the two sets of magnets (shifted and non-shifted) are shifted half a slot pitch, resulting

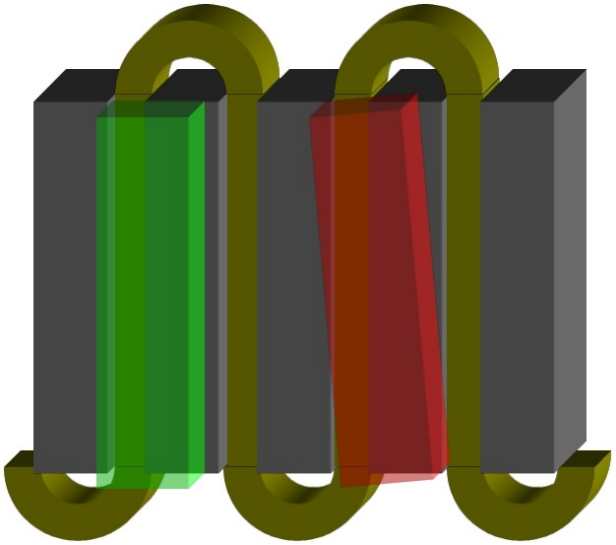

Fig. 32: Paralleled (green) and skewed (red) magnet

in equal but opposite directed cogging force.

Shifted Angular Position Between the Rotor Discs: In axial flux machines, there are often two or more rotor discs. By shifting the angular position of one disc to another, results in the same achievement as the unsymmetrical rotor in the previous section. The possibility to shift the angular position has no limitation, whereas for the latter approach the magnet leakage flux is influenced and setting a limitation on the shift in magnets. Assembling the motor with skewed rotor plates might be difficult due to high magnetic forces trying to align them, which must be considered and taken into account during the design.

Fractional Slotting: Another approach to achieve low cogging is to have a different amount of poles in rotor and stator. The result of this is that the number of slots per pole per phase, q, is not an integer, and the cogging force at each magnet is different. In this case, the cogging forces on one magnet are eliminated by another magnet in the machine, resulting in a very low cogging torque. This is not applicable to the design in this report, because the fractional slotting requires a two-layer coil winding.

Due to the possibility of a very high q, the cogging force generated is initially low. By introducing one or more of the techniques mentioned above, the cogging would be decreased to a satisfying value. The most promising methods to be applied are a combination of skewed magnets, and offset angular position of the rotor plates. If the cogging is still too high, the air-gap flux density has to be lowered. A 3D-FEM simulation must be used to find the minimum cogging torque and at the same time calculating the THD in the back-EMF waveform with the different methods described above.

XIII. Manufacturing and assembling the stator prototype

In order to investigate the practical challenges regarding the coil design, a stator prototype is built and tested. The objective is to show that a three phase machine can be produced, insulated, and work as a motor. The prototype is financed by Greenway Energy AS, and manufactured at Finmekanisk verksted in Realfagsbygget. The electrical and geometrical parameters are chosen to fit the DNV Fuel Fighter motor. In that way, the same housing, shaft, rotor, and test equipment can be used. The stator prototype is shown in Fig. 33. The main design parameters are displayed in table III.

TABLE III:
Design parameters

Description	Symbol	Value
Outer magnet diameter	M_{Do}	$320mm$
Inner magnet diameter	M_{Di}	$210mm$
Axial depth of coil layer	C_d	$4mm$
Gap between conductors in active area	C_g	$0.5mm$
Number of stator poles	p	48
Number of stator layers	C_{lay}	2
Number of turns per phase per pole	q	1
Number of phases	ph	3
Rated rotational speed	n	$270rpm$
Rated induced voltage ph-n rms	e_{ph}	$14.4V$

An iron free wave-winded topology is chosen because of its simplicity and lack of inter-phase connectors. The stator has two separate three phase layers, where each phase has one turn in each layer, resulting in two turns per phase. The stator has 48 poles and one turn per phase per pole. The axial depth of the coil layer is $4mm$, resulting in a total stator axial depth of $8mm$ plus insulation between the layers. The motor is an in-wheel axial flux internal stator topology, where the housing and the rotor are its moving parts, while the stator and shaft are standing still. The magnets used in this machine are laid in a Halbach array, with $45°$ shifted magnets. The magnet axial depth is $15mm$, and the total airgap is $10.7mm$, measured from magnet to magnet. The air gap magnetic field from the Halbach array is highly sinusoidal, and has its peak at $1.05T$. A full study on this motor can be found in the master theses of John Ola Buøy at the institute of Electric Power Engineering [26]. John Ola has designed the high performance axial flux motor which was used in this years Shell Eco Marathon race, having a theoretical efficiency at 97.7%, and measured 96.3% at rated speed and load.

A. SolidWorks and dimensions

Based on the electrical and geometrical dimensions given in table III, the remaining parameters, which are needed for the SolidWorks design, are calculated in the following text. Fig. 35 displays the coil geometry with parameter description.

The inner and outer diameter of the coil active area are chosen to be equal to the inner and outer magnet diameter.

$$C_{Do} = M_{Do} \tag{17}$$

$$C_{Di} = M_{Di} \tag{18}$$

resulting in an active length C_L of

$$C_l = \frac{C_{Do} - C_{Di}}{2} = 55mm \tag{19}$$

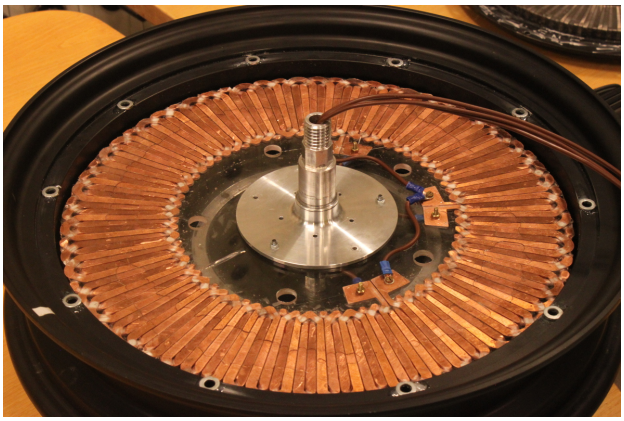

Fig. 33: Finished stator prototype (one layer)

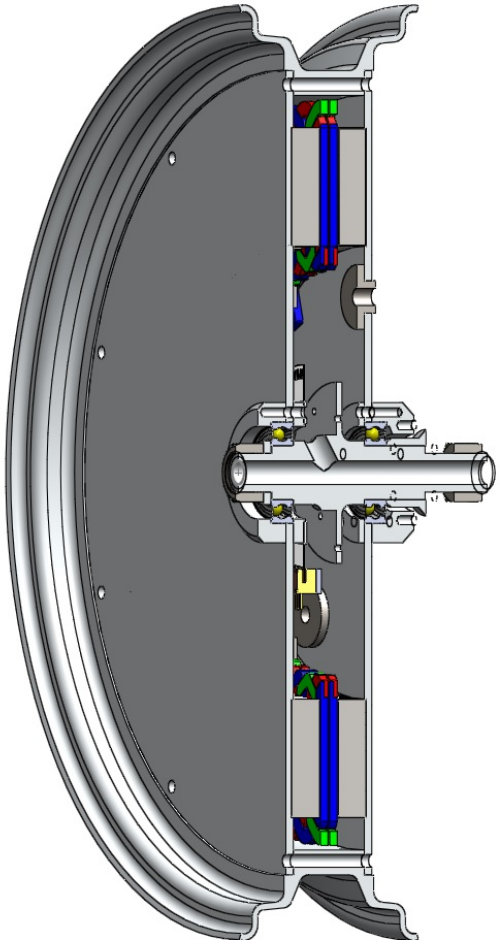

Fig. 34: SolidWorks Section View of DNV Fuel Fighter Motor

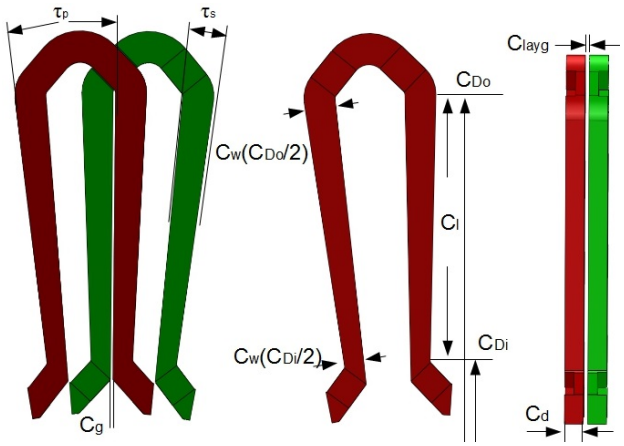

Fig. 35: SolidWorks Design Parameters

and the ratio between inner and outer diameter, K_D, given as

$$K_D = \frac{C_{Di}}{C_{Do}} = 0.65625 \tag{20}$$

K_D is an important parameter in the optimization of the machine, but also highly dependent on mechanical constraints and machining possibilities. Its usual range is 0.55 to 0.75 for medium sized machines, and 0.9 to 0.95 for MW sized machines.

The average radius, r_{avg}, is used to calculate machine performance in the analytical model. The average radius is given as

$$r_{avg} = \frac{C_{Do} + C_{Di}}{4} = 132.5mm \tag{21}$$

The pole pitch τ_p and slot pitch τ_s are usually expressed as length, $[mm]$. But because of their dependence on the radius it is more convenient to express them as an angle in radians

$$\tau_p = \frac{2\pi}{p} = 0.1309(= 7.5^\circ) \tag{22}$$

$$\tau_s = \frac{\tau_p}{ph \cdot q} = 0.0436(= 2.5^\circ) \tag{23}$$

The conductor width is dependent on the radius. This is due to a constant gap between the conductors in the active area, defined as C_g. For the SolidWorks design, it is convenient to find the conductor width at D_o and D_i. Using trigonometry calculations over a triangle spanning half a slot pitch, the conductor width at radius r is defined as

$$C_w(r) = 2r\,tan(\frac{\tau_s}{2}) - C_g \tag{24}$$

and the conductor widths at inner and outer diameter are calculated to be

$$C_w(\frac{C_{Do}}{2}) = 6.48mm \tag{25}$$

$$C_w(\frac{C_{Di}}{2}) = 4.08mm \tag{26}$$

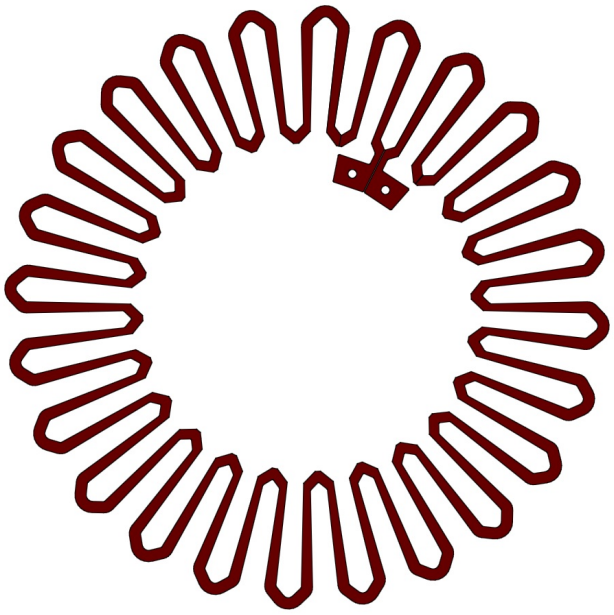

Fig. 36: Wave winding of a single phase

When calculating current densities and using 2D-models, the average conductor width must be used:

$$C_w(r_{avg}) = \overline{C}_w = 5.28mm \tag{27}$$

The fill factor in this design is very high, and for a single stator layer it can be calculated from the unused active volume

$$k_{fill} = 1 - \frac{C_g\, C_l\, q\, ph\, p}{\pi\left[(\frac{C_{Do}}{2})^2 - (\frac{C_{Di}}{2})^2\right]} = 91.9\% \tag{28}$$

The ratio of end coil volume versus total conductor volume is calculated using SolidWorks. In this design the end coil represents 30%. Increasing the number of poles and larger K_D will contribute to an even lower end coil volume, but due to mechanical and geometrical constraints it is difficult to achieve.

The entire winding of a phase is manufactured as one piece, as shown in Fig. 36. The winding for each phase is similar in shape, but there are two different versions of the machined cuts. To be able to successfully assemble a stator layer, it is important where the machined cuts are placed. This is illustrated in Fig. 37, where the red winding has all its cuts on one side, while the blue winding has alternating cuts on two sides. The last winding, which is not shown in the picture, is identical to the red winding but flipped.

The connectors on the winding are placed symmetrically two pole pitches apart. This is shown in Fig. 38, where two windings are laid on top of each other, but shifted two pole pitches. The negative connection in one layer is then positioned directly above the positive connection in the second layer. The same can be done for any number of layers, providing an easy method to connect all layers together to one phase winding. The finished SolidWorks design of the stator is shown in Fig. 39.

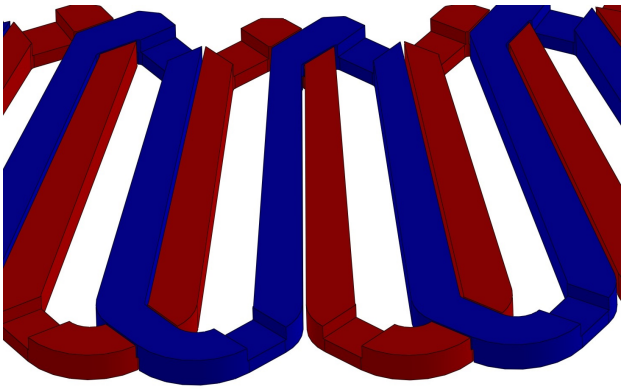

Fig. 37: Machined cuts in two of three phase windings

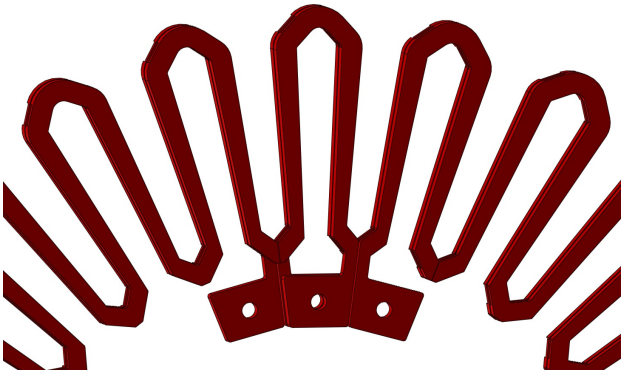

Fig. 38: Connection between different layers

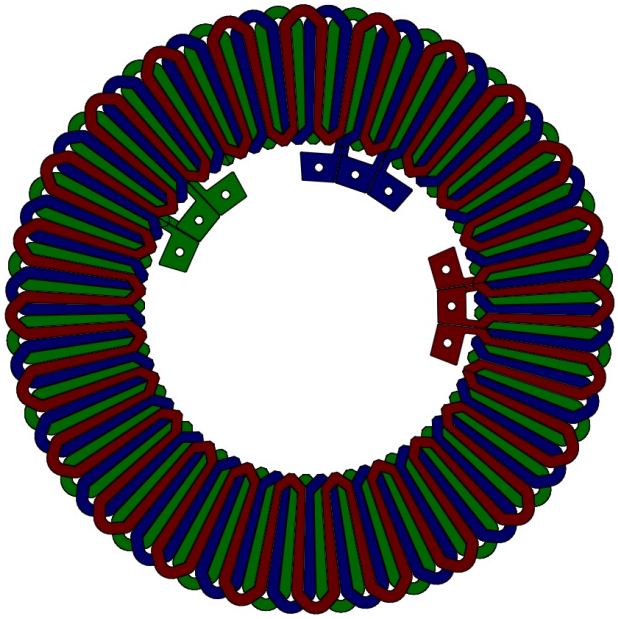

Fig. 39: Finished SolidWorks Design

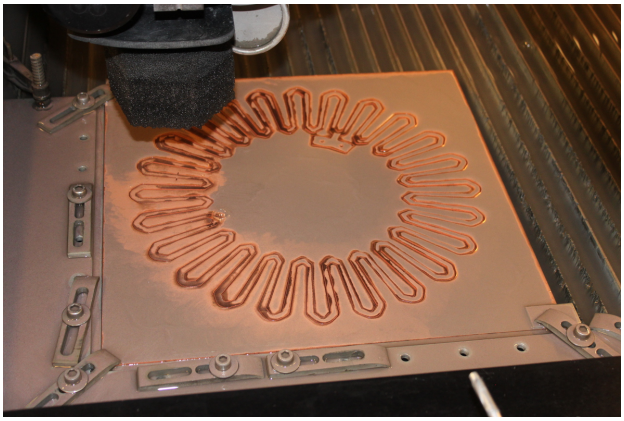

Fig. 40: Water-cutting the copper plates

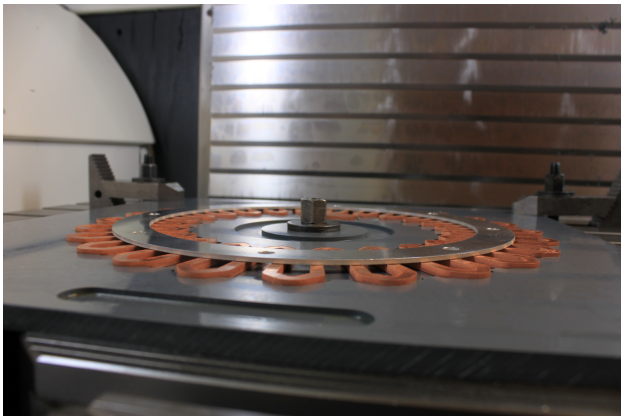

Fig. 41: Inside the CNC miller

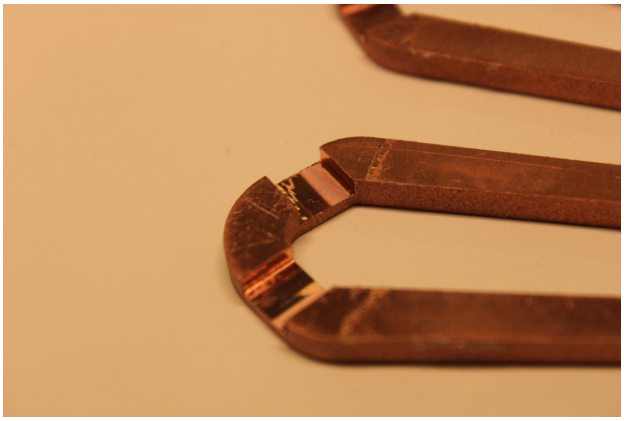

Fig. 42: Machined cuts on upper end coil

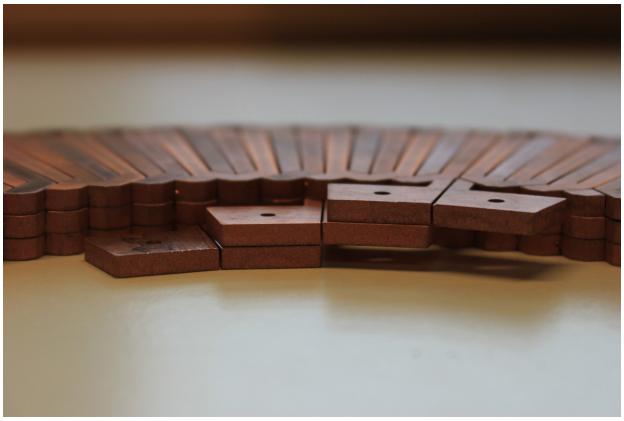

Fig. 43: Three coil layers connected in series

B. Workshop manufacturing

Based on the design in SolidWorks, the stator was manufactured by Øystein Hagemo at Finmekanisk verksted in Realfagsbygget.

The original plan was to use aluminum as conductor material, but because of difficulties finding the suitable aluminum alloy within a reasonable time frame, there was no other choice than to use copper. A $1000X2000X4mm$ copper plate was purchased, which was enough to manufacture ten wave-windings, giving three coil layers.

1) Water cutting: The first step in the process is to water-cut the copper plates. The estimated total cut length of one wave-winding is about $8m$, which take $26min$ at the selected speed quality and $11.5kg$ of abrasive sand. Fig. 40 shows a finished wave-winding inside the water cutter.

2) Machined cuts: The second step is to use a CNC miller to make the machined cuts on the windings. A mold is made to hold the winding still during the manufacturing. The mold is made of plastic, where the wave-winding shape has been milled half-way into its surface. On top, an aluminum ring is used on to force the winding into the mold. The mold, with a wave-winding inside, is shown in Fig. 41. In the future, it is recommenced to use aluminum instead of plastic, and steel instead for aluminum, for the mold. This is because of vibrations during milling. A picture of the machined cuts can be seen in Fig. 42.

3) Finishing manufacturing: The third step of the process is to use a band saw to cut the connectors in two, because it was left connected to provide better stability during the manufacturing. In Fig. 43 three stator layers are shown, and in Fig. 44 a top view of the stator is shown.

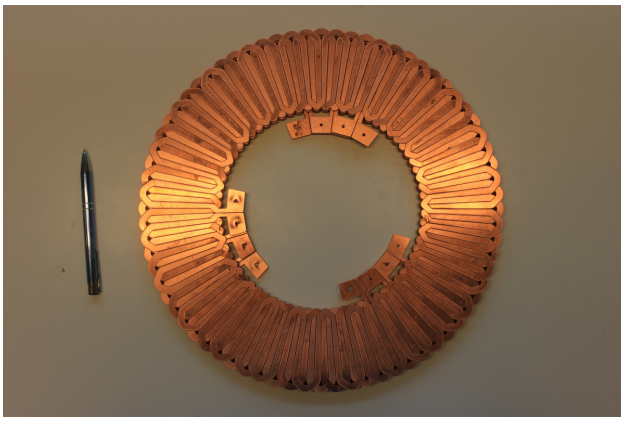

Fig. 44: Overview stator prototype

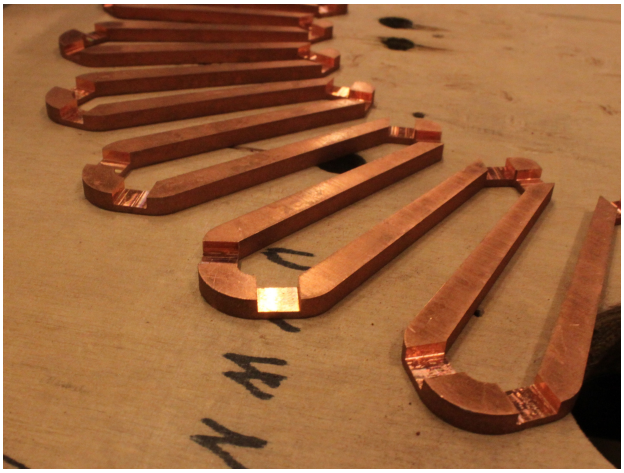

Fig. 45: Machined cuts before rubbing down

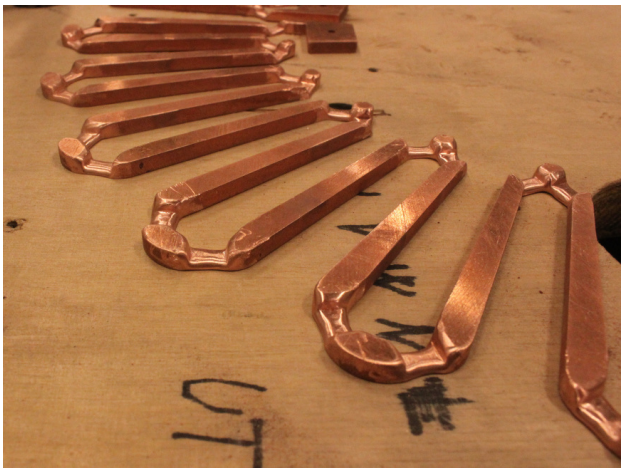

Fig. 46: Machined cuts after rubbing down

C. Insulation

In order to use the windings in a motor, the wave-windings must be electrically insulated from each other. The procedure is to use electrical insulation tape, and insulate just the machined cuts. To fit insulation in the cut, it was made larger than the necessary width. The margin was chosen to be $0.5mm$, leaving $0.25mm$ for insulation on either side. The tape used is a 3M glass cloth tape ordered from Farnell[25]. With a thickness $0.177mm$, it is within the margin set by the machined cuts. The dielectric strength was tested in a vice, where two connectors were pressed together with insulation tape between them. The dielectric strength was measured to be in the area of $4kV$ with one layer of tape.

The insulation process proved possible, but very difficult and time consuming to complete. Because of the sharp edges produced by the CNC miller, and a too narrow cut in the coil, the tape got torn during assembling. Another method would be to use an insulation coating, but it would not successfully insulate the sharp edges. Both approaches would be sufficient if the machined cuts were larger and rounded, leaving no edges. It can easily be implemented while machining the cuts in the CNC miller.

To overcome the insulation problem, the sharp edges had to be rubbed down using sand paper. Two pictures showing before and after applying sand paper, are shown in Fig. 45 and 46. After rubbing down the sharp edges, electrical insulation tape is applied.

The tape is cut to the width of the conductor and laid in to layers in the coil cut. The two layers form an X, where one is placed along the conductor and one is wrapped around. A close up picture of this can be seen in Fig. 47. The method is used on both upper and lower end winding as seen in Fig. 48. The tape will insulate the entire cut, and it is not necessary to insulate more than half on the machined cuts in a complete layer.

Using tape as an insulator is very time consuming and not applicable to commercial manufacturing. The best method here is to widen the machined cuts and manufacture a plastic

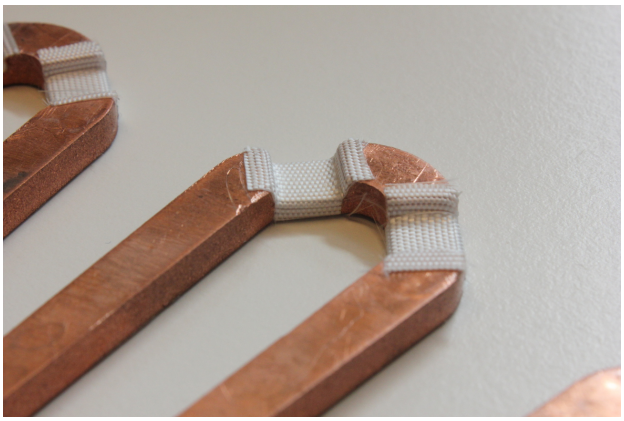

Fig. 47: The insulation method, two tape layers in an X

Fig. 48: Section of a fully insulated winding

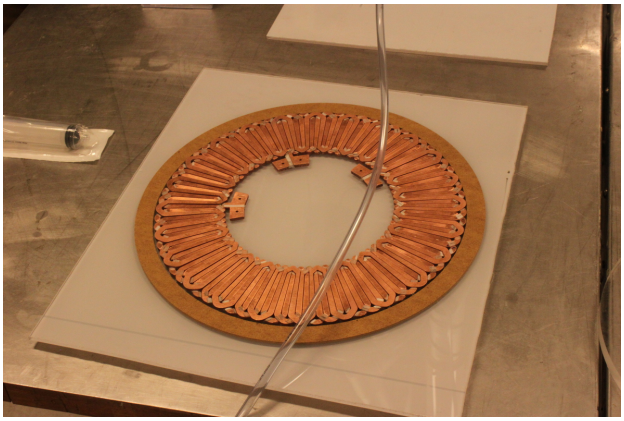

Fig. 49: The mold used for casting with epoxy

Fig. 50: A number of vices is used to compress the mold to leave a thin epoxy layer on the stator

holder that fits the conductor inside the cut, providing electrical insulation and strong mechanical strength.

D. Casting the stator

The next step in the process is to cast the stator in epoxy. This was done with the help from the Shell Eco Marathon group. Only one stator layer is molded at a time. Because of the flat design, the mold is very simple. Two plates of plexiglas are used on top and bottom of the stator layer. Around, a cardboard ring is used, with a slightly lower height than the stator layer. A picture of the mold with an insulated stator layer inside is shown in Fig.49. The finish on the epoxy after molding is dependent on the finish of the mold, and using plexiglas the casted stator will have a smooth and clear surface.

The best method of casting the stator is to use vacuum pump to circulate the epoxy into the mold while extracting all air and air bubbles inside. But due to the lack of experience and the simplicity of the mold, the epoxy was simply pored onto the stator. Before applying the epoxy, it was situated inside a vacuum chamber which extracted most of its air to limit the amount of bubbles. When filling the mold with epoxy and cover it with the plexiglas, the epoxy will flow out over the cardboard. When applying pressure on the mold, only a thin layer of epoxy will remain on top of the stator.

To ensure that the entire stator is filled with epoxy, a syringe is used to insert more epoxy through a hole in the middle of the mold. However, this proved difficult and the result led to a number of big bubbles in the center area of the stator. The preferred method would be to overfill the mold with epoxy before closing the mold with the plexiglas.

In Fig. 50 the epoxy has been inserted into the mold and vices are used to press the mold together and force epoxy out over the cardboard. The epoxy uses about a day to set. The stator is easily extracted from the mold, and the cardboard is cut away by hand.

E. Machining bolts and shaft holes

The next step is to machine holes in the epoxy to fit the shaft, bolt holes for the fastening for the flange holding the stator, and holes for large screws used to assemble the rotor

Fig. 51: Milling the shaft hole, where the center of the geometry is found

Fig. 52: Completed stator prototype

TABLE IV:
Parameters, iron free model

Description	Symbol	Value
Outer coil diameter	C_{Do}	$320mm$
Inner coil diameter	C_{Di}	$210mm$
Ratio between inner and outer diameter	K_D	0.65625
Axial depth of coil layer	C_d	$4mm$
Gap between conductors in active area	C_g	$0.5mm$
Number of stator poles	p	48
Number of stator layers	C_{lay}	2
Gap between stator layers	C_{layg}	$0.7mm$
Total stator depth	C_{totd}	$8.4mm$
Number of turns per pole per phase	q	1
Number of phases	ph	3
Rated rotational speed	n	$270rpm$
Rated induced voltage ph-n rms	e_{ph}	$14.4V$
Magnet axial depth	M_d	$15mm$
Magnet remanent flux	B_r	$1.3T$
Total airgap axial depth	g	$10.7mm$
Active coil length	C_l	$55mm$
Average coil radius	r_{avg}	$132.5mm$
Pole pitch	τ_p	$0.1309rad$
Slot pitch	τ_s	$0.0436rad$
Average conductor width	$\overline{C_w}$	$5.28mm$

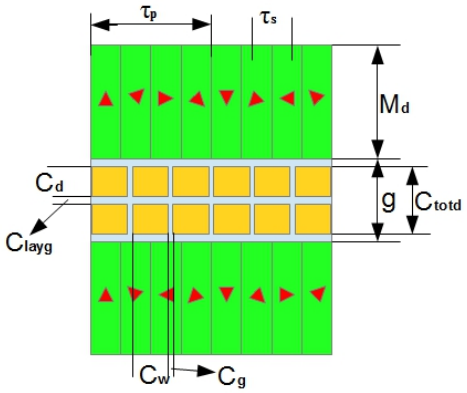

Fig. 53: 2D model at r_{avg}

plates. This work was done using CNC milling, as shown in Fig. 51. The stator prototype is now finished and ready to be tested. The insulation is tested between the phases to withhold $250V$, which is much higher than the rated voltage. A finished stator layer is shown in Fig. 52.

XIV. Analytical model iron free

Given the SolidWorks design of the stator prototype, an analytical model is created to calculate its expected performance. The main parameters are given in table III, along with the calculated values in the previous section. The parameters used in this model are rewritten in table IV. A 2D-geometry of the motor is shown in Fig. 53 where the geometric parameters are plotted.

A. Magnetic flux density

The air gap magnetic flux density is needed to perform calculations on the design. The magnets are assembled as a

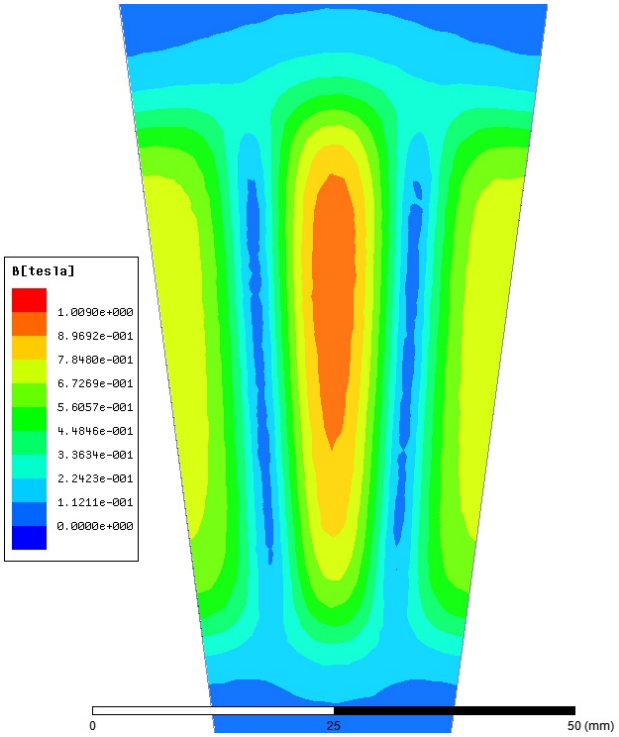

Fig. 54: 3D air gap flux density

Halbach array with $45°$ shifted magnetization. The remanent flux density is $1.3T$.

Because of the Halbach array, it is difficult to calculate the airgap flux analytically. A 3D Maxwell simulation is done in order to determine how the flux density is flowing in the air gap. The field plot, in the middle of the air gap, is shown in Fig. 54. The Hallbach array produces a varying magnetic flux, with higher flux density at the middle of its pole and towards the outer diameter.

Fig. 55 is showing the flux density on a straight line, from inner diameter C_{Di} to outer diameter C_{Do}, through the center of the pole. The peak flux density is occurring at $145.8mm$ from the center, which is at 90% of C_{Do}.

In Fig. 56 the air gap magnetic flux density is plotted on a circumferential line at a constant radius at r_{avg}. It shows that the magnetic field is varying sinusoidally between its poles, which contributes to a low THD in the back-EMF.

B. Torque constant

The magnetic field is defined by the radius, from Fig. 55, and angle, from Fig. 56, as $B(r, \theta)$. The equation defining the torque at a differential radius dr is given by

$$T = I_{ph} N\, p \int_{\frac{C_{Di}}{2}}^{\frac{C_{Do}}{2}} B(r,\theta)\, r\, dr \tag{29}$$

which is the torque at one pole pitch with the RMS phase current I_{ph}.

To simplify the calculation, the flux density is defined as $\hat{B}(r)cos(\theta)$, where θ is the position of the conductor away

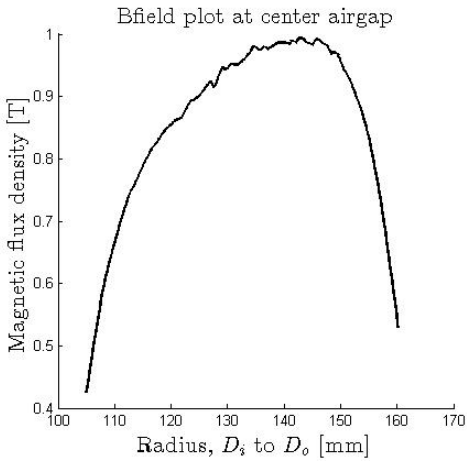

Fig. 55: Line plot at maximum flux density

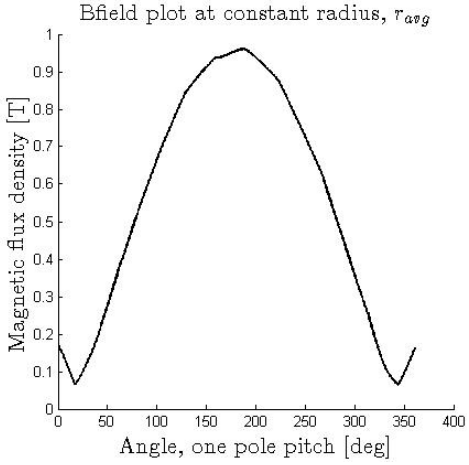

Fig. 56: Line plot of flux density at constant radius

from the center pole, and $\hat{B}(r)$ is the peak flux density at radius r from the data in Fig. 55.

max K_T: When a phase is conducting peak current, $\sqrt{2}I_{ph}$, it is situated in the magnetic field $\hat{B}(r)cos(0)$. At the same time, the other two phases are conducting half their peak current, and both situated in the magnetic field defined as $\hat{B}(r)cos(\tau_s)$. This situation has the highest electrical loading, and therefore the highest torque constant. The torque constant is found by

$$\frac{T}{I_{ph}} = \sqrt{2}C_{lay}\, q\, p(1 + cos(\tau_s)) \sum_{r=\frac{C_{Di}}{2}}^{\frac{C_{Do}}{2}} \hat{B}(r) r \Delta r$$

yielding a torque constant equal to

$$K_T^{max} = 1.7138\, Nm/A$$

min K_T: The minimum electrical loading occurs when one of the phases are conducting zero current, leaving the other two phases with a phase current of $\sqrt{2}I_{ph}cos(pi/6)$. In this situation, the two conductors are situated in the magnetic field defined as $\hat{B}(r)cos(\tau_s/2)$. The torque constant is calculated as

$$\frac{T}{I_{ph}} = 2\sqrt{2}cos(\pi/6)C_{lay}\, q\, p\, cos(\tau_s/2) \sum_{r=\frac{C_{Di}}{2}}^{\frac{C_{Do}}{2}} \hat{B}(r) r \Delta r$$

yielding a torque constant equal to

$$K_T^{min} = 1.4846\, Nm/A$$

avg K_T: The average torque constant is then calculated, resulting in the average torque production of the machine, along with a torque ripple between the maximum and minimum electrical loading.

$$K_T = \frac{K_T^{max} + K_T^{min}}{2} = 1.5992\, Nm/A \tag{30}$$

$$K_T^{ripple} = \frac{K_T^{max} - K_T^{min}}{2} = 0.1146\, Nm/A \tag{31}$$

which can be expressed as

$$K_T(t) = K_T + K_T^{ripple} sin(3\omega_{el} t) \tag{32}$$

where ω_{el} is equal to $2\pi f_{el}$, and f_{el} is the electrical frequency.

C. Induced back-EMF

When the motor is rotating, a voltage is induced in the winding. The magnitude can be calculated using flux-linkage, calculated by the amount of flux through a pole span in the middle of the air gap, together with the rotational speed of the motor. The time dependent induced voltage can be calculated as

$$EMF(t) = \frac{d\lambda(t)}{dt} = N\frac{d\Phi(t)}{dt} = \omega_{el} N \hat{\Phi} cos(\omega t) \tag{33}$$

Assuming sinusoidal varying magnetic field at radius r, as in Fig. 56, the magnetic flux is then defined as $\hat{B}(r)/\sqrt{2}$, where $\hat{B}(r)$ is defined as peak air gap flux density from the values in Fig. 55. The peak flux $\hat{\Phi}$ is then defined as $\hat{B}(r)/\sqrt{2}A(r)$. The peak induced voltage for a phase at a rotating speed n can be calculated as

$$\begin{aligned} \hat{EMF} &= \omega N \hat{\Phi} \\ &= n\frac{2\pi}{60}\frac{p}{2}\, q\, p\, C_{lay} B(r,\theta) A(r) \\ &= n\frac{\pi p^2}{60}\, q\, C_{lay} \left[\int_{\frac{C_{Di}}{2}}^{\frac{C_{Do}}{2}} \frac{\hat{B}(r)}{\sqrt{2}} \tau_p r\, dr \right] \\ &= n\frac{\pi p^2}{\sqrt{2}\,120}\, q\, C_{lay} \tau_p \sum_{r=\frac{C_{Di}}{2}}^{\frac{C_{Do}}{2}} \hat{B}(r) r \Delta r \end{aligned}$$

where N is the number of turns in a phase winding and ω_{el} is the electrical rotating speed defined as $[rad/s]$. From this equation, the torque constant for RMS induced voltage per rotating speed n is found to be

$$K_E = 0.0997\, V/rpm \tag{34}$$

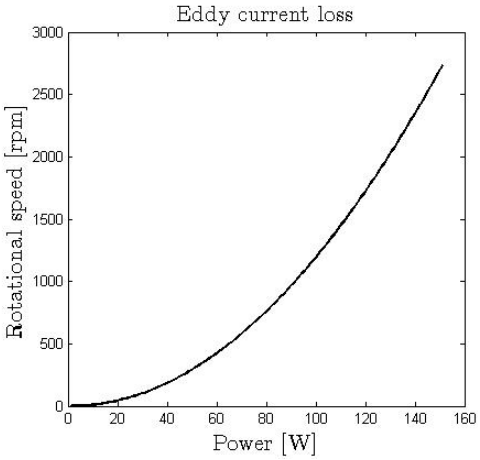

Fig. 57: Eddy current loss

D. Rotational losses

Due to solid conductors, the stator will experience very large induced eddy currents, and are dominating the rotational losses that occurs in the motor. The big conductors act like a magnetic brake on the rotating magnets, and contributes to high losses. The eddy currents can be calculated using the time averaged power loss pr volume equation [24]

$$P_e = \frac{\omega_{el}^2 w^2 B_m^2 \sigma}{24} \ [W/m^3] \tag{35}$$

where B_m is the peak magnetic flux density at a sinusoidal shaped air gap flux, w is the width of the conductor facing the magnets, and σ is the conductivity of the conductor material.

The equation in (35) is used to calculate the eddy current loss in the design. The volume where the eddy currents are acting is given by the active stator conductor volume.

$$V_{eddy} = C_w C_l C_d C_{lay} q\, p\, ph \tag{36}$$

The total eddy current loss at rotational speed n, in a thin circumferential slice at radius r, with the peak magnetic field defined from Fig. 55 as $\hat{B}(r)$, is given as

$$dPe = \frac{(\frac{\pi p}{60} n)^2 C_w(r)^2 \hat{B}(r)^2 \sigma_{cu}}{24} C_w(r) C_d q\, p\, ph\, C_{lay} dr$$

from $r = D_i/2$ to $D_o/2$. Where $C_w(r) = 2r\, tan(ts/2) - C_g$. The equation is simplified to

$$dPe = k\, n^2 (2r\, tan(\frac{\tau_s}{2}) - C_g)^3 \hat{B}(r)^2 dr \tag{37}$$

$$k = \frac{\pi^2}{60^2 24} p^3 \sigma_{cu} C_d q\, ph\, C_{lay}$$

The total eddy current loss can then be calculated as

$$P(n) = k\, n^2 \sum_{r=D_i/2}^{D_o/2} (2r\, tan(\frac{\tau_s}{2}) - C_g)^3 \hat{B}(r)^2 \Delta r \tag{38}$$

By dividing (38) with the motor rotational speed ω_{mech}, a eddy current torque constant ("braking torque") is found from the slope of this curve

$$K_{eddy-torque} = \frac{d}{dn} \left[\frac{P(n)}{n \frac{2\pi}{60}} \right] = 1.0455\, Nm/rpm \tag{39}$$

E. DC-resistance

The conductor resistance is calculated by the equation

$$R = \frac{l}{\sigma A} \tag{40}$$

where l is the length, σ is the conductivity, and A is the cross-section of the conductor. Using the parameters from the design, the active area and the end-winding area resistance are calculated.

The resistance of conductors in a winding, situated in the active area of the stator, is calculated as

$$R_{active} = \frac{C_l}{\sigma_{cu} \overline{C}_w C_d} q\, p\, C_{lay} = 4.1662 m\Omega \tag{41}$$

The resistance in the end coil area is difficult to calculate due to the geometry, and an approximation must be used. To find the lengths, it is assumed that the length of the upper and lower end coils are equal to six times the slot pitch. The cross section in the end coils are varying due to the machined cuts. Assuming that the depth of the coil is half the depth to the active area, and that the width of the cross section is the average conductor width. The upper end coil resistance of a winding is then calculated to be

$$R_{end-coil}^{upper} = \frac{6\tau_s \frac{C_{Do}}{2}}{\sigma \overline{C}_w \frac{C_d}{2}} q \frac{p}{2} C_{lay} = 3.1730 m\Omega \tag{42}$$

the lower phase end coil resistance is calculated as

$$R_{end-coil}^{lower} = \frac{6\tau_s \frac{C_{Di}}{2}}{\sigma \overline{C}_w \frac{C_d}{2}} q \frac{p}{2} C_{lay} = 2.0823 m\Omega \tag{43}$$

and total winding resistance is then calculated to be

$$R_{DC} = R_{active} + R_{end-coil}^{upper} + R_{end-coil}^{upper} = 9.4215 m\Omega \tag{44}$$

F. AC-losses

There are mainly two contributers to the AC-losses in this design. The skin effect and proximity effect. The skin-effect is the phenomena where the current in a conductor tends to flow at the outer area of its conductor, due to the magnetic field set up by its own current. The loss is included in the design by increasing the DC-resistance of the winding. The proximity effect is eddy currents induced in a conductor, because of a time-varying magnetic field set up by a neighboring conductor. The loss is calculated and included as a P_{prox} term in the AC-losses. [24]

Because of the low frequencies, and dominating eddy currents from the magnets, the AC-losses are neglected.

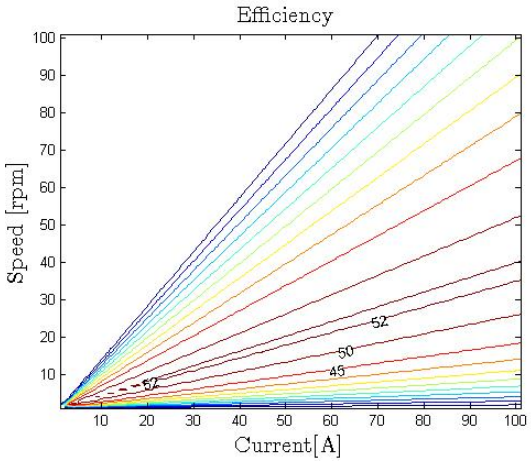

Fig. 58: Analytical efficiency

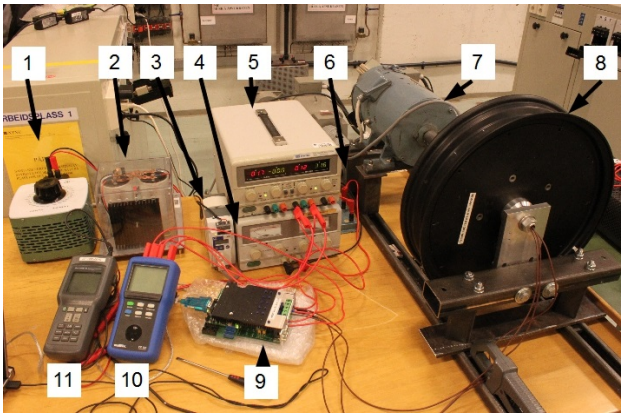

Fig. 59: Laboratory setup, look in table V for information

G. *Efficiency*

From the torque constant, the efficiency may be calculated. The efficiency is defined by the shaft power and the power supplied to the motor.

$$\eta = \frac{P_{shaft}}{P_{in}} \tag{45}$$

The power output on the shaft, and power supplied to the motor by the following equations.

$$\begin{aligned} P_{shaft} &= P_{out} - P_{rot-loss} \\ &= (K_T I_{ph} - K_{eddy-torque} n)\, n \frac{2\pi}{60} \\ P_{in} &= K_T I_{ph} n \frac{2\pi}{60} + 3R_{dc} I_{ph}^2 \end{aligned} \tag{46}$$

The efficiency is calculated for a large range for the phase current I_{ph} and the rotational speed n. The result is shown in Fig. 58. The maximum efficiency is 52%. The figure clearly shows that due to the rotational loss from the eddy currents, a minimum amount of current is needed to have positive shaft power.

A number of losses, not accounted for in the analytical calculations, will reduce the efficiency. At this stage in the design process, any more accurate result is abundant.

XV. Laboratory testing of stator prototype

The finished stator was tested using the housing, shaft, and equipment belonging to the Shell Eco Marathon group. Their stator is designed with Litz-wires, and optimized to have an extremely high efficiency.

Assembling the rotor magnets were problematic, and as a result, the air gap between the rotor plates became to small to fit two coil layers. The testing was therefore conducted using only one stator layer, but due to symmetry, the results can be multiplied with two to represent both layers.

The stator was terminated in a star connection, and a temperature probe was fitted on one of the connectors in the neutral point - to provide measurements on the temperature inside the motor. The motor was run using a position sensor, where the control algorithm and the power electronics circuit board were delivered by Smart Motor AS. With the position sensor, it is ensured that the prototype motor always runs at the optimal angle.

During the lab experiment, the motor prototype was tested as a generator with open terminals, motor at no-load condition, blocked rotor condition, and load condition. From this the speed dependent induced voltage, the loss due to eddy currents and the torque constant were found. Due to very high eddy current losses, limited power supply and air cooling of the stator, the prototype could not be tested at rated torque.

After the lab testing it was found that the torque sensor was defect. The shaft going through the sensor was unaligned, and giving fluctuated measurements at stand still and low speed.

The rotational losses were measured by inserting a dummy stator, but the torque sensor proved too unreliable and the results were inconclusive. Compared to the amount of eddy current loss in this prototype, the rotational losses are neglectable.

Fig. 59 shows an overview of the laboratory setup, and information about each component can be found in table V. Various equipments are used to measure voltages and currents. Additionally to the equipment in the figure, an oscilloscope was used to measure voltage and current wave-forms entering the motor, and displayed the measurements from the torque sensor. A was tachometer used to find the rotating speed of the motor whenever the position sensor was disconnected.

A DC motor is connected on the shaft together with the prototype motor. It is used to brake or speed the test motor in the various experiments. Its field winding is supplied through a DC-power source, while its anchor winding is supplied from the grid through a variac and a diode rectifier.

A. *Stator resistances*

The test motor is connected to the power supply by long cables. The phases are terminated as a star inside the motor, with a neutral cable leading out of the motor, so that phase

TABLE V:
Laboratory equipment list

Ref.	Type	Description
1	Variac	Control voltage on the DC-motor stator winding
2	Diode rectifier	Rectifying AC voltage from variac to DC voltage
3	Torque display	Reads the output from the torque sensor on the shaft
4	DC power supply	Feeds the field winding in the DC-motor
5	DC power supply	Feeds the power electronics on the motor controller
6	DC-motor terminals	Switchboard for field and stator winding in the DC-motor
7	DC-motor	Used to brake or spin the test motor
8	Test motor	The in-wheel electric motor, with prototype stator inside
9	Motor controller	Transforms DC to AC power to the test motor
10	Watt-meter	Measure power, voltage and current to the motor controller
11	Grid analyzer	Measures the power, voltage and current into the test motor
–	Oscilloscope	Used to analyze the current, voltage and torque waveforms
–	Tachometer	Measuring the rotational speed of the test motor
–	Temperature sensor	A konstantan copper temperature sensor is fitted inside the test motor

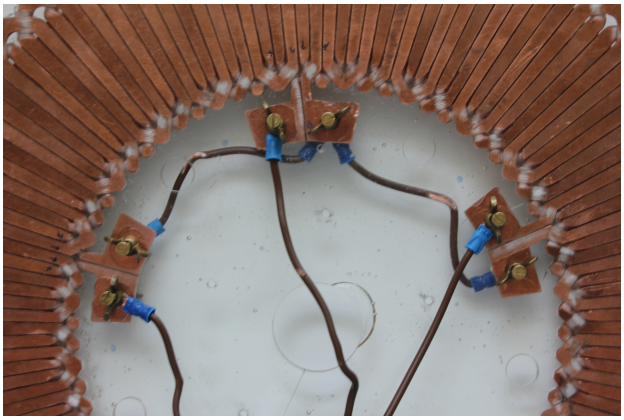

Fig. 60: Star-connected stator

to neutral measurements can be conducted. The star point is located on the phase 2 terminal. The setup is shown in Fig. 60.

A measurement of the DC-resistances on the test stator was conducted, and the results are given in table VI. The measured values for R_{ph-ph} and R_{ph-n} are done from the end of the phase cable to the neutral point. The average phase resistance is found from these values to be

$$R_{ph-n} = 21.845m\Omega \tag{47}$$

TABLE VI:
Stator resistances

$R_{ph-ph}[m\Omega]$		$R_{ph-n}[m\Omega]$		$R_{winding}[m\Omega]$	
Ph1-Ph2	43.56	Ph1-N	22.49	Ph1	5.674
Ph1-Ph3	44.80	Ph2-N	20.90	Ph2	5.488
Ph2-Ph3	43.52	Ph3-N	22.41	Ph3	5.385
avg	43.96	avg	21.93	avg	5.516

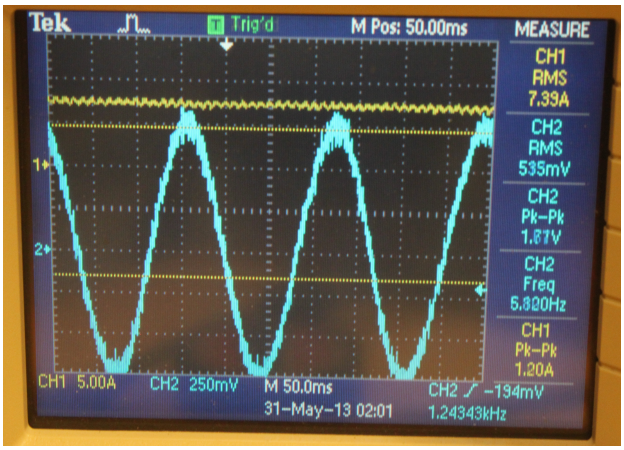

Fig. 61: Induced voltage, phase to phase

The $R_{winding}$ is measured over the connectors of a single phase, and is showing the resistance in the copper winding itself. From this, the average winding resistance without cables is measured to be $5.516m\Omega$. The resistance is higher than expected, but it is including the screw connectors as seen in the picture. The actual resistance is about $4.778m\Omega$, which was tested on a copper winding before epoxy was applied, when the measurement could be done without connectors. Compared with the analytically calculated winding resistance of $9.4215m\Omega$ for two layers, the error is only 1.427%.

B. Generator mode, open terminals

The first test is to rotate the prototype motor with the DC motor. The terminals on the motor is open, and the oscilloscope is connected between one of the phases and the star neutral point. The induced voltage is noted for several speeds, but due to large eddy current losses, the speed is limited to $20rpm$. The results are shown in table VII, and plotted in Fig. 62. In the figure, the black line is the measured data while the red line is a least-squares fit. From the fitted red line the voltage constant K_E is found:

$$K_E = 18.0843mV/rpm \tag{48}$$

Comparing with the analytically calculated K_E of $99.7mV/rpm$ for two layers, the result is 63% off, which is very high. Reducing the peak magnetic flux density in the analytical model to 72.6% of its value, converge the results.

The induced back-EMF is highly sinusoidal, and is shown in Fig. 61.

TABLE VII:
Induced back-EMF voltage

Speed [rpm]	Voltage ph-n RMS [mV]
0	0
4.3	100
8	160
15.4	300
19.4	370

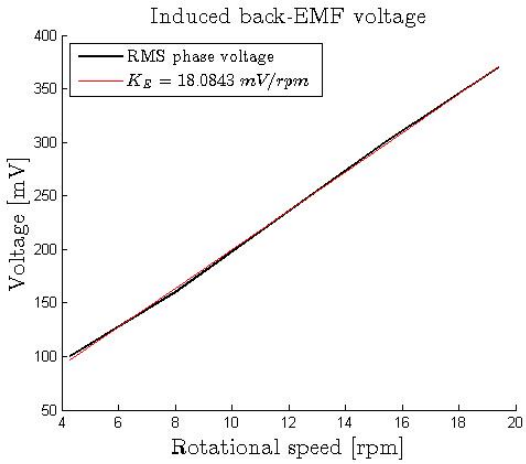

Fig. 62: Back-EMF voltage

C. No-load condition

In the No-load condition, the AC-losses are calculated. The main contributor to this loss is the eddy currents in the conductors, but eddy currents in magnets, higher rotational losses due to speed and skin effect due to high frequency, are also contributing.

The prototype motor is now connected to its power supply, and the DC-motor is unconnected. The rotational torque loss on the shaft is measured to be $0.16Nm$. The measured values in this test are voltage, current, and power entering the motor, and together with the rotational speed, the loss due to eddy currents may be found.

The measurements are given in table VIII, but due to limitations on the grid analyzer, the power could not be measured at $5rpm$, so the data at that speed is disregarded from the further work.

To find the AC-losses, the DC-losses must be subtracted.

TABLE VIII:
Power loss during no-load condition

Speed $[rpm]$	Phase voltage rms $[mV]$	Phase current rms $[A]$	Phase power $[W]$
0	0	0	0
5	500	2.8	0
10	600	7	3
15	800	10.3	7
20	900	14	12
25	1100	17.4	18
30	1300	21	26
35	1500	23.2	33
40	1600	27.5	44

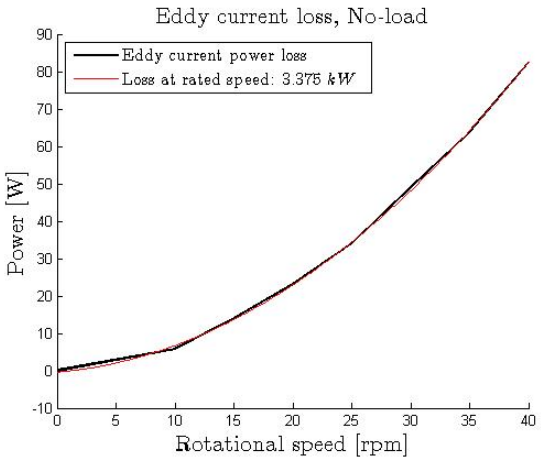

Fig. 63: Eddy current losses

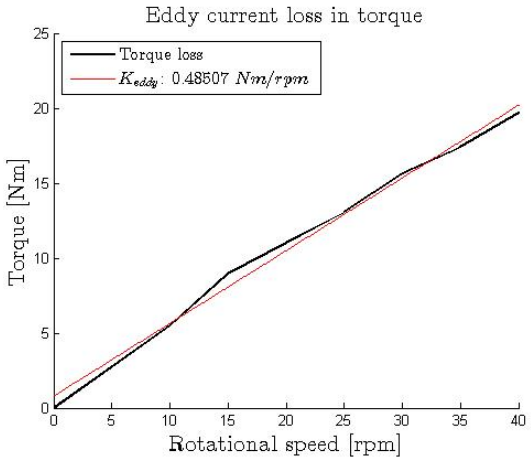

Fig. 64: Torque loss due to eddy currents

The DC-losses are resistive losses from the phase resistance, using the average phase - neutral resistance found in table VI, and the phase line current, the power loss is calculated and subtracted in the result.

The AC-losses are plotted in Fig. 63, where the black line represents the measured values, and the red line is a least-squares fit. Using the fitted red line, the AC-losses at rated speed is $3.375kW$.

By dividing the supplied motor power by the rotational speed ω_{mech}, the output torque lost due to the AC-losses may be calculated. In Fig. 64 the torque versus speed is plotted, and using the least-squares fitted red line, the torque constant loss due to AC-losses is calculated to be $K_{eddy} = 0.48507Nm/rpm$. The analytically calculated eddy current torque constant is $1.0455Nm/rpm$ for two layers. Comparing these results, the error is 7.2%, which is relatively close.

It was expected that the AC-losses found in the laboratory was higher than the analytical model, due to the circumferential flux occurring from the magnet to magnet leakage flux.

TABLE IX:
Shaft torque, blocked rotor

Phase current rms $[A]$	Shaft torque $[Nm]$
0.9	1.2
3.2	2.22
5.2	3.7
7	4.7
8.9	5.6
10.8	7

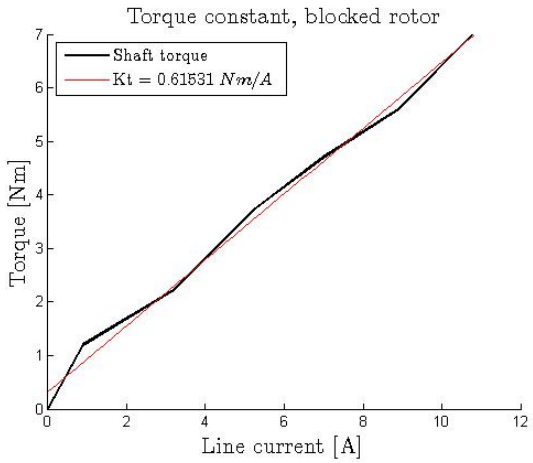

Fig. 65: Torque konstant, blocked rotor

D. Blocked rotor test

In the blocked rotor test, the rotor is blocked from rotating. The stator is supplied current, and the torque sensor will measure the torque produced on the shaft. From this, the torque constant can be found. The results are given in table IX and plotted in Fig. 65, where the black line is the measurements and the red line is a least-squares fit.

The torque sensor had difficulties to measure the torque at stand still, and was giving different results depending on the position of the rotor. In the figure it is clear that the measurements do not give the perfect straight line as expected. The torque constant is calculated to be

$$K_T = 0.61531 Nm/A \tag{49}$$

The calculated torque constant is $1.5992 Nm/A$ for two layers, yielding an error of 29.95%. By reducing the peak flux density in the analytical model to 77%, the results converge.

E. Load test

The DC-motor is now connected to a resistance, and the field winding is powered. When the test motor is rotating, the DC-motor will act as a generator, and braking the shaft. In this way, the torque sensor will measure the output power from the test motor and the grid analyzer measures the input power. The rotating speed, line current, shaft torque, and phase input power are measured and displayed in table X.

The efficiency is dependent on the speed of the motor and the line current. Using the shaft torque and the input power

TABLE X:
Measurements, load test

Speed $[rpm]$	Phase current rms $[A]$	Shaft torque $[Nm]$	Phase power $[W]$
10	7	0.44	3
20	14.7	0.64	12
10	19.3	8	14
20	27.7	8	32
40	29	1.12	46

TABLE XI:
Efficiency

Speed $[rpm]$	Phase current rms $[A]$	Efficiency $\eta(speed, current)$
10	7	5.12%
20	14.7	3.72%
10	19.3	19.95%
20	27.7	17.45%
40	29	3.40%

from the table, the efficiency can be calculated. The result is shown in table XI. Due to very large AC-losses, the efficiency is very low, as expected.

To find the maximum efficiency of this motor, the results from the previous sections can be used. The torque generated by the stator current is given by the torque constant in 49. The DC-losses are calculated by using the average phase-neutral resistance in 47 and phase current. The AC-losses are speed dependent, and the fitted curve from the no-load test is used. The efficiency is then calculated using a Matlab script, over a large speed and current range. The result is plotted in Fig. 66, where a contour plot of the efficiency is shown. The contours are plotted with a 2.5% step. The maximum efficiency is about 25% at $120 rpm$ and $170 A$. The losses at this state are calculated to be $2.6 kW$, and is too high considering that the motor is air-cooled.

From the figure, it can be seen that states with a high speed, but at low currents, are outside the capability zone of the motor. This is due to the need for a minimum amount of current to overcome the eddy current braking at a certain speed.

F. Laboratory conclusion

The prototype stator was analytically investigated before the laboratory testing, and as presented in this section, some of the predictions was wrong.

The phase resistance proved to be very reliable, the measured resistance in a coil was $4.778 m\Omega$, giving the analytical model an error of 1.427%.

The torque and voltage constant prediction was too high, as the error in both were about 30%. The AC-losses, where the induced eddy currents from the magnets is dominating, where measured to be 7.2% lower than the analytical result. It was anticipated that the AC-losses would be much higher than the analytical result, since only axial directed flux was investigated to determine the induced currents, while the AC-losses in the lab would include both axial and circumferential flux, in addition to other losses. However, reducing the airgap

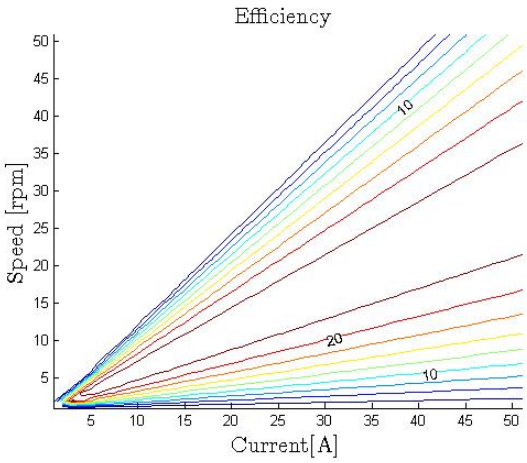

Fig. 66: Calculated efficiency [%]

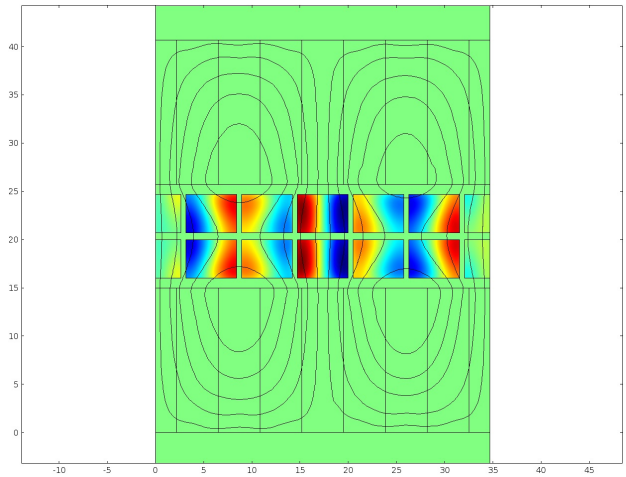

Fig. 67: Induced eddy currents in conductors. Without iron

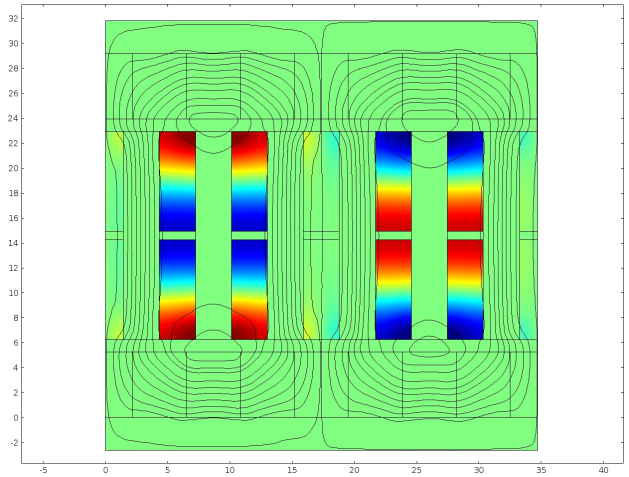

Fig. 68: Induced eddy currents in conductors. With iron

magnetic field in the analytical model with 30%, the torque and voltage constant would converge with the laboratory results. The calculated induced currents would be reduced to only 50% if its originally calculated value, but now the laboratory result is higher than the analytical and satisfies its prediction.

This proves that the air gap flux used in the analytical model was too high. The reason for this can be a difference in material properties in the magnet datasheet compared to the actual magnet performance, and that the air gap was slightly increased due to difficulties in assembling the Halbach array.

XVI. Iron stator

The iron free topology of the stator design is not suited for industrial applications. The wide conductors lead to a very high eddy current loss, which in turn, limits the speed and efficiency of the motor. By reducing the conductor width, and introducing laminated iron in the gap between conductors, the eddy current loss due to the magnet flux will be reduced.

In order to preserve the torque performance of the motor, the magnetic and electric loading must remain the same. Electric loading is dependent on the total conductor cross section, so when the width of the conductor is reduced due to iron, its axial length is increased. The magnet loading is dependent on the average air gap flux. When iron is introduced in the stator, the effective airgap is significantly reduced, and the magnet depth can be reduced to maintain the same magnetic loading. In the iron free topology, Halbach array magnets was used to remove the need for back iron, but in an industrial application of this design, conventional back iron and magnet array is used.

This section investigates the different impacts on the machine due to the introduction of iron. In the nest section, an analytical model is presented.

A. Induced eddy currents in conductors due to rotating magnets

A COMSOL simulation is done to visualize the effect of iron in the machine, regarding induced currents in conductors due to rotating magnets. To be able to compare results, the design used for the iron free prototype is altered to contain iron.

The induced current in the conductors for the iron free design is shown in Fig. 67. In Fig. 68, the induced current for a design with iron at the same electrical and magnetic loading, is presented. In both designs Halbach array are used, and in the iron model, the magnet size is reduced while the axial length of the stator is increased, as mentioned in the introduction.

The eddy currents induced by the magnets in the iron free design was due to both axially and circumferential directed flux. With iron in the stator, the axially directed flux is now traveling through the iron, instead of the conductors, but the circumferential flux is still present. A quick calculation shows that the iron-free design has an eddy current loss of $962W$, while $28.2W$ with iron, at $50Hz$ ($125rpm$), which is an improvement of 97%.

In order to further reduce the induced currents in the conductors, the two coil layers in Fig. 68 can be divided up

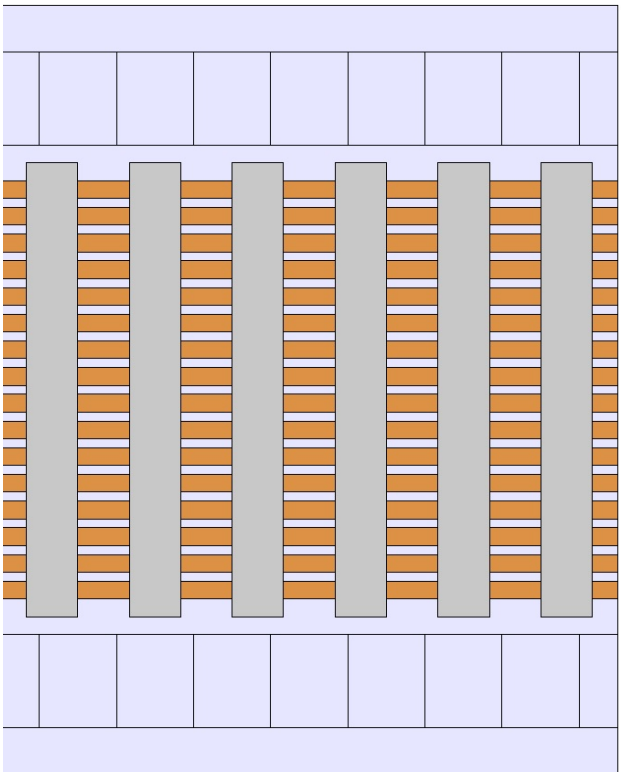

Fig. 69: 2D model, with extended lamination axial depth, 16 coil layers, and Halbach array

into several thin layers. In practice it is possible to manufacture very thin wave-windings, but less than $1mm$ is difficult. Based on this, a new model is created, where the total conductor cross section is divided into 16 individual layers, with a conductor depth of $1mm$, enabling the same electrical loading as previously. The power loss due to eddy currents are now reduced to $8.9W$.

About 86% of the power dissipation is located in the conductors facing the air gap, where a substantial axial directed flux component is attacking the conductors before entering the lamination. By increasing the lamination length to go into the air gap by $1mm$ beyond the conductors, the total resistive loss due to eddy currents, is reduced to $1.98W$. A figure of this model can be viewed in Fig. 69.

The induced eddy currents was calculated using COMSOL with frequency study. The frequency study varies the absolute value of the air gap magnetic flux in each position in a sinusoidal wave form. This is not accurate enough to be used to retrieve the real eddy current loss, since a time dependent study with rotating stator or rotor should be used. However, the results gathered here are still valid to investigate the effects of iron in the stator, where the real value of the induced current will have the same, or close to, the amount of reduction as the frequency study implies. By implementing the design with a small C_g, many layers and extended lamination depth, the eddy currents due to the magnets will be reduced to a neglectable level.

B. Induced eddy currents due to stator leakage flux

Using thin coil layers with the extended lamination length, will reduce the eddy currents due to rotating magnets to a negligible level. However, introducing iron in the stator will increase the stator leakage flux, which influences the skin-effect and proximity effect. Here, a design with conventional back iron and magnet array is used to investigate the impact on the machine. The magnetic and electric loading remains the same as in the original iron free design, equal to the models in Fig. 67 and Fig. 68, but with two stator layers and extended lamination axial depth. The test was conducted by applying $8A$ peak current into phase 1, with $50Hz$ electrical speed. The result with and without iron are plotted in Fig. 70 and Fig. 71.

The effects at this current and frequency are very small, but the difference between the models can still be compared. Due to the iron, phase 2 and 3 are shielded from the magnetic flux set up by phase 1, hence neglectable proximity effect. Without iron, the loss due to the proximity effect from phase 1 is $0.95mW$, and $1.6\mu W$ with iron. The skin effect is measured by comparing the change in phase resistance at DC power and AC power, in the current conducting phase. Without iron, the increase in resistance due to skin effect is 4.23%, while 45% with iron. Because of the iron, the slot leakage flux is significantly higher than the iron free model, hence the skin effect is larger.

The skin effect is the induced eddy currents from a variable magnetic field inside a current carrying conductor, where the magnetic field is set up by its own current. The flux which is causing this effect is the stator leakage flux, and it attacks the conductors in a circumferential direction. The power loss associated with the eddy currents are proportional to the third of the conductor depth, $P_{skin-eff} \propto C_d^3$. By using the design presented in Fig. 69, the skin effect is reduced, and represents a resistance increase of 7.23%.

The introduction of iron in the stator increases the stator produced flux, hence, the stator leakage flux. Further investigation of this phenomena will not be done in this thesis, but it is highly recommended to accurately determine its effect through a 3D model.

C. Induced currents in laminations

Due to the axial directed flux from the magnets, and the circumferential directed flux from the stator and magnet leakage flux, the iron inside the slot will induce eddy currents. Because of this, it is important how the iron is laminated. In Fig. 72, the flux components that are attacking the lamination are drawn as red, and the induced currents in green. To reduce the losses, it is recommended to make the surfaces facing the magnetic fields as small as possible, the recommended method to laminate the iron is shown in the top end of the figure.

D. Induced eddy currents in magnets

Conventional magnets and back iron are used in this design to highlight the losses occurring in the magnets due to laminations in the stator. The magnet will experience higher flux den-

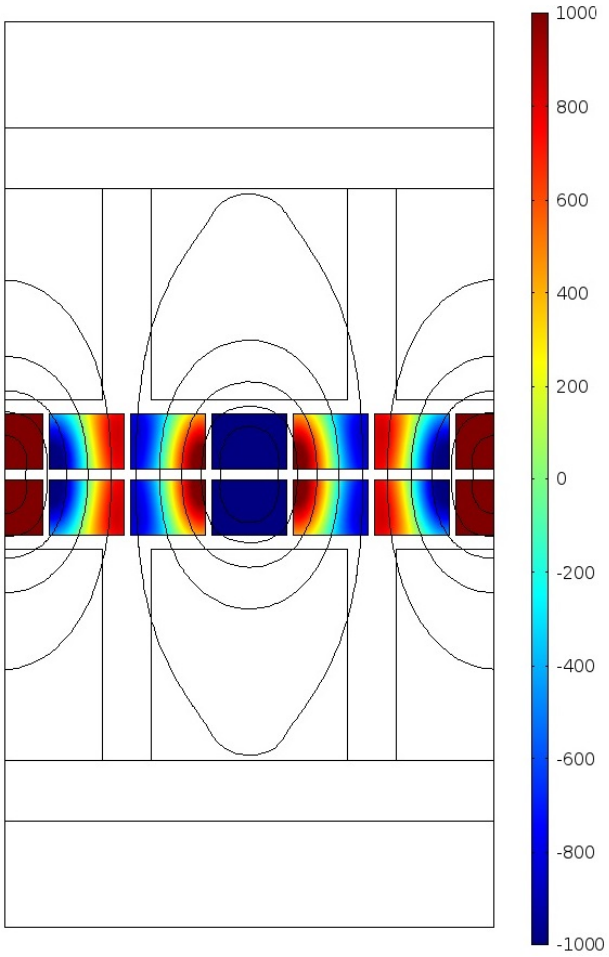

Fig. 70: Proximity effect without iron, 8A pk phase current in phase 1, $50Hz$

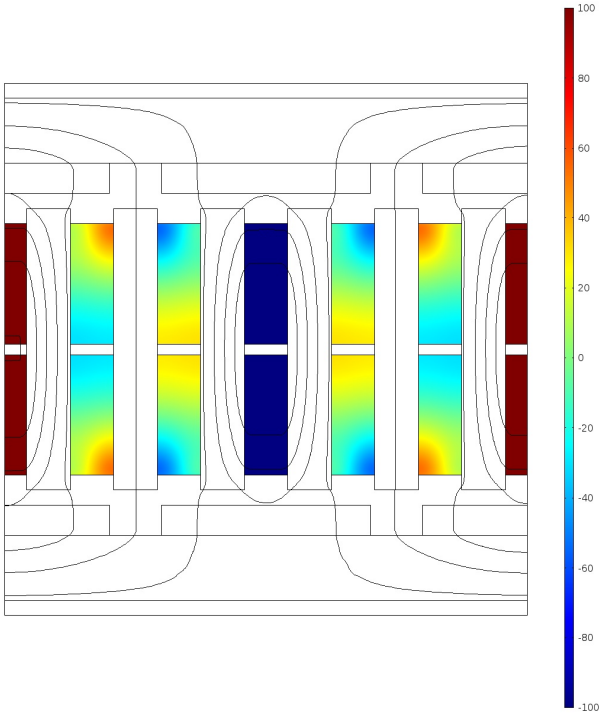

Fig. 71: Proximity effect with iron, 8A pk phase current in phase 1, $50Hz$. (The color range here is ten times smaller than in Fig. 70)

sities in areas underneath the laminations, as shown in Fig. 73. The position of these flux concentrations moves, as the magnet is rotating, and a variation in magnetic flux is created. From this, circulating eddy currents are induced inside the magnets, contributing to losses. The effect of this phenomena is not substantial, due to relatively low conductivity in the magnet. However, it represents an internal heat source, and if not taken into account, may lead to high operational temperatures inside the magnet. At high temperatures, the magnet becomes weaker, and in combination with high electrical loading, the magnet might become permanently demagnetized during a short period of time.

The induced current and its direction inside the magnet are shown in Fig. 74. To limit the losses, the magnet should be made up of a number of smaller magnets, which are electrically insulated from each other, in order to reduce the surface area where the induced currents can flow. The recommended method to ”laminate” the magnet is shown in the figure.

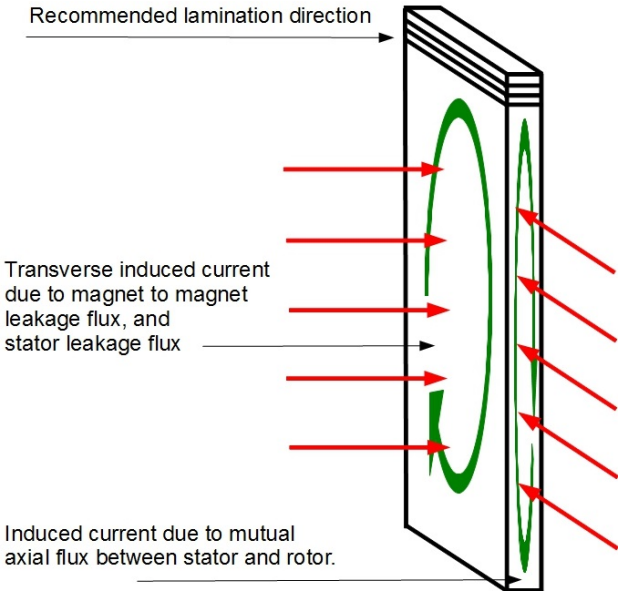

Fig. 72: Induced eddy currents in lamination pack

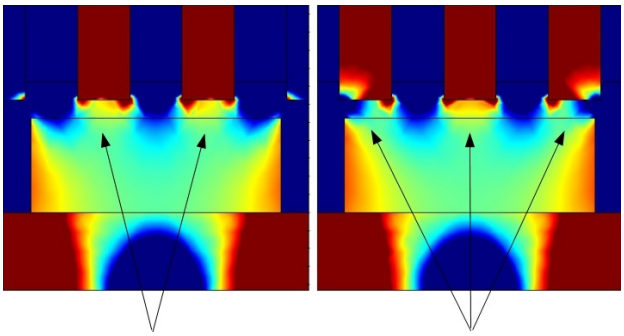

Fig. 73: Magnetic flux consentration in magnets due to laminations

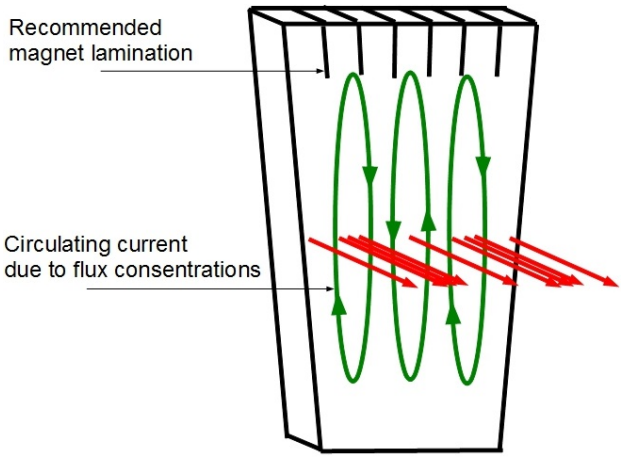

Fig. 74: Induced current in magnet

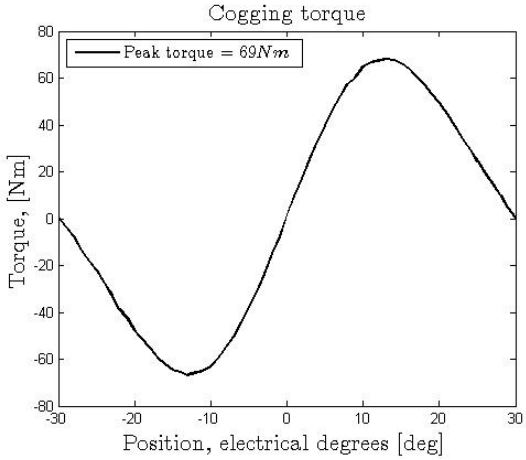

Fig. 75: Cogging torque in base design

E. Cogging torque

When iron is introduced in the stator, the magnets will experience a force due to variation in magnetic reluctance. To investigate this phenomena, a simple 2D linear model is made in COMSOL, with iron lamination and back iron. In the design there are three laminations per pole pitch, which implies that the cogging torque waveform spans one period in $60°$ electrical degrees. The simulation is done by magnetostatic sweep from $-30°$ to $30°$ electrical degrees, where $0°$ is at the stable detent position shown to the right in Fig. 73. The unstable detent positions, at $\pm 30°$, are shown to the left. The cogging torque calculated for this design is plotted in Fig. 75. The cogging is varying nearly sinusoidally, with its peak value at $69Nm$.

In a well designed motor, the cogging torque should be minimized. The methods to reduce the cogging was presented in section XII, and now some of these methods are tested on this design.

Magnetic wedges: By using magnetic wedges fitted in the stator slots, the change in reluctance torque is reduced, hence, the cogging torque is reduced. Since the lamination stacks are designed to exceed the conductors out into the air gap, the additional length can be fitted with iron.

The simulation shows that the cogging is reduced to zero, and the torque production at $8A$ rms phase current has been reduced from $14.5Nm$ to $13.3Nm$. However, the magnetic wedges strongly increases the magnet to magnet leakage flux and stator leakage flux, and thereby influences the AC-losses in the machine. The air gap cooling channel is no longer in contact with the conductors, and only interior cooling channels are available. Because of this, the magnetic wedges must be carefully designed if used.

Shifting angular position of rotor plates: It is possible to reduce the cogging torque by shifting the angular position of the rotor plates. This has been done by shifting the upper rotor disk to the right, and the lower rotor disk to the left, with $\theta_{shift}/2$ electrical degrees. The result is shown in Fig. 76, where minimum cogging occurs at $\theta_{shift} = 30°$, reduced by 81.2%. The minimum cogging occurs at this angle, because the rotor plates has been shifted one half period of the original cogging torque waveform. Where it had maximum cogging, is now a dentent position, but, since the waveform was not pure sinusoidal, the resulting cogging torque does not equal to zero.

Varying magnet position: By shifting the positions of the magnets on the rotor disks, the peak cogging torque will occur at different angles at their respective magnet, hence, the total cogging torque will be reduced. This is done by shifting the position of the magnets with $\theta_{shift}/2$ electrical degrees. The north poles are shifted to the right on the upper rotor disk, and to the left on the lower rotor disk. The south poles are shifted opposite compared to the north poles. In this way the magnets are all shifted equally off their original position, securing constant torque production.

The results are shown in Fig. 77. The minimum cogging occurs at $\theta_{shift} = 20°$, with a 86% reduction. However, the

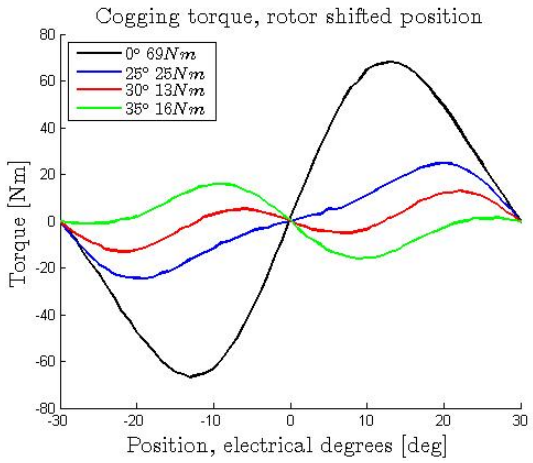

Fig. 76: Reduced cogging due to shifted rotor positions

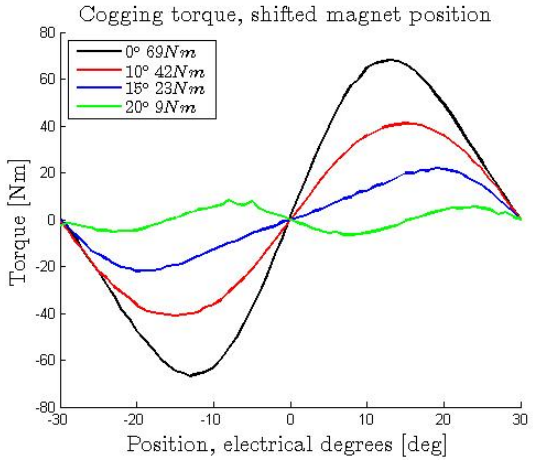

Fig. 77: Reduced cogging due to shifted rotor positions

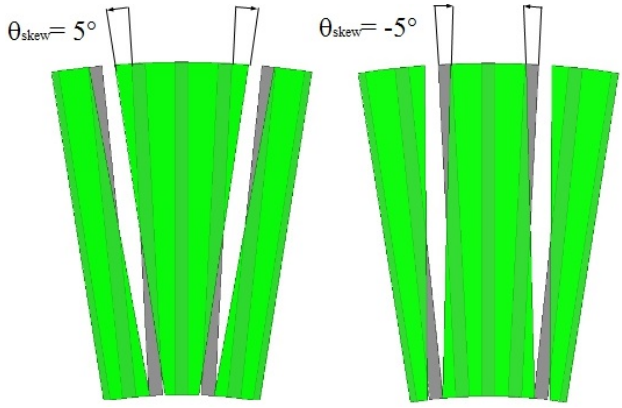

Fig. 78: Shaping magnets in 3D, two pole pitch sector

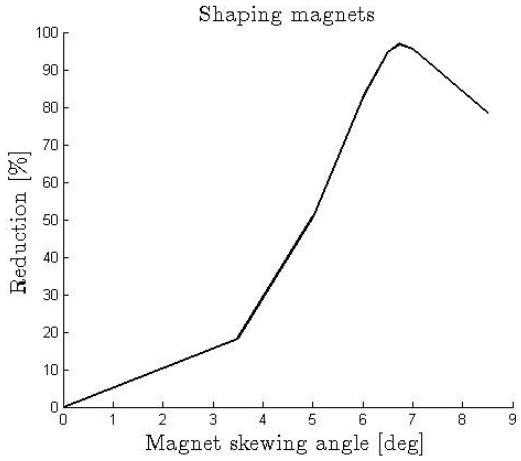

Fig. 79: Cogging reduction at various skew angles

practical limitation of this method is about $10°$ shift, due to magnet to magnet leakage flux. Because of this, the method presented here can only be used in combination with other techniques.

Shaping the magnet: Another approach to reduce the cogging is to change the shape of the magnet, so not the entire length of the magnet reaches the edge of the lamination at the same time. The original width of the magnet is defined by the function

$$M_w(r) = \alpha_m \tau_p r \tag{50}$$

where α_m is equal to the ratio between magnet and pole pitch, τ_p is the pole pitch, and r is the radius from center. A skew angle is defined, which says how many degrees the magnet side length is shifted from its original position. This is shown in Fig. 78, where the skew angle is $5°$ in the first figure, and $-5°$ in the second.

3D maxwell magnetostatic was used to calculate the torque for several skew angles swept between $\pm 30°$ electrical. The cogging torque at each skew angle was compared to the original cogging torque at zero skewing. The percentage decrease in cogging torque is shown in Fig.79, and an optimum skew angle is identified at $6.75°$, having reduced the cogging with 97%.

It is difficult to find a suitable method to reduce the cogging, and since it also reduces the torque output, it must be carefully studied. The cogging torque is highly geometrical dependent, and for any variation in the model, the minimum cogging optimization must be re-initiated. However, it has been proven here that it is possible to reduce the cogging to an acceptable level.

F. Air gap magnetic flux

When iron is introduced in the stator, the air gap magnetic flux will change, which has a great impact on the machine performance. A 3D model of the design is made in Maxwell, and the air gap magnetic field produced from the magnets are calculated. A field plot at center air gap is shown in Fig. 80. The laminations strongly influences the magnetic field strength at their position, and can clearly be seen in the figure by the radially red lines, and in Fig. 81 as peaks in the air gap flux waveform.

Compared to the sinusoidal air gap flux created by the Halbach array, the introduction of iron in the stator will produce highly non-sinusoidal induced voltages in the back-

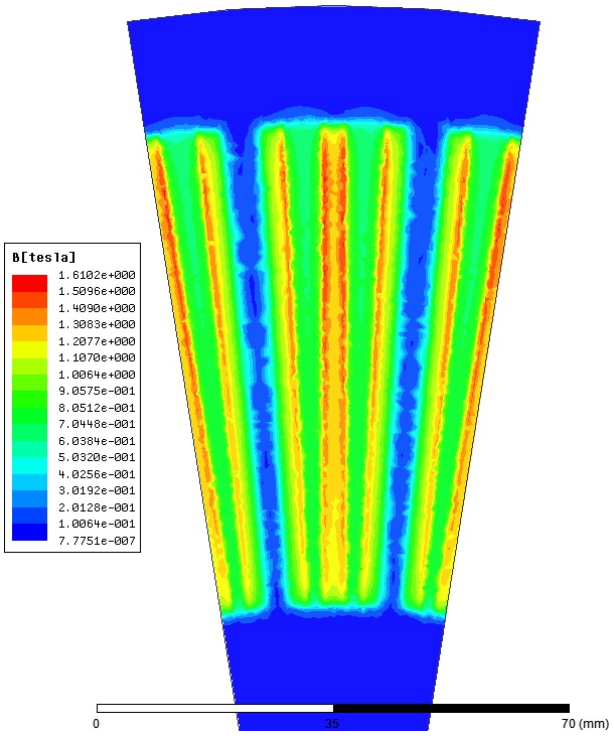

Fig. 80: Air gap magnetic flux density

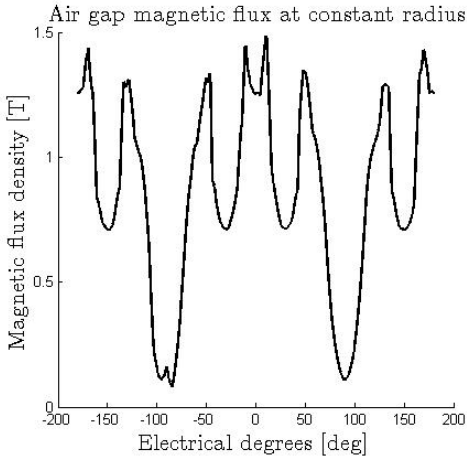

Fig. 81: Air gap magnetic flux density at average radius

EMF. The effect can be lowered through the various techniques used to reduce the cogging torque, but should still represent a difficult challenge to adopt iron in the design.

In Fig. 82 the air gap flux is plotted along a radial line in the middle of the center pole. The magnetic flux is higher toward the outer diameter of the magnet, but the difference is much lower than observed for the iron free stator.

Magnetic loading in iron stator: When analytically calculating the air gap flux, neither the variation in radial direction, nor the highly disoriented air gap flux waveform, are accounted

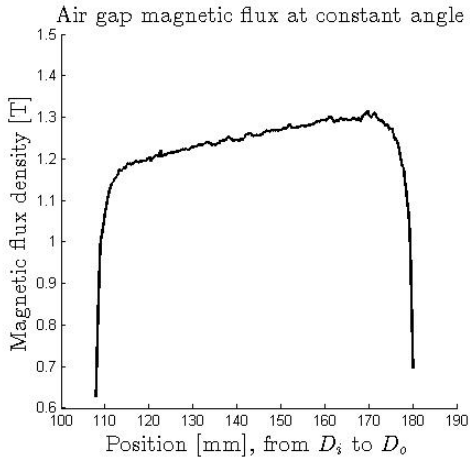

Fig. 82: Air gap magnetic flux density in a straight line at center pole

for. The analytically peak air gap flux density as [2]

$$\hat{B}_m = \frac{B_r}{1 + \frac{g}{l_m}\frac{A_m}{A_g}} \tag{51}$$

where $\hat{B}_m$ is the peak air gap flux density, B_r is the remanence flux in the magnet, g is the air gap length, l_m is the magnet length, A_m is the magnet cross section area, and A_g is the air gap cross section area.

The magnet cross section area can be calculated as

$$A_m = \alpha_m \tau_p r_{avg} C_l \tag{52}$$

where α_m is the ratio between magnet and pole pitch, τ_p is the pole pitch measured in radians, r_{avg} is the average radius, and C_l is the stator active length.

The air gap cross section area is given by the total iron area facing the magnet. The ratio of iron present in the air gap cross section area can be calculated as

$$R_{iron} = \frac{L_w}{\overline{C}_w + L_w} \tag{53}$$

where L_w is the lamination width, and $\overline{C}_w$ is the average conductor width. The air gap cross section area can then be calculated as

$$A_g = R_{iron} \tau_p r_{avg} C_l \tag{54}$$

The average air gap flux density, B_g, can be calculated from (51) by assuming that the peak flux density is constant over the magnet surface

$$B_g = \frac{\tau_m \hat{B}_m}{\tau_p} = \alpha_m \hat{B}_m \tag{55}$$

Combining these equations and using the parameters from the 3D model, the flux passing from the magnets and into the stator can be calculated as

$$\Phi = \frac{\alpha_m B_r}{1 + \frac{g}{l_m}\frac{\alpha_m}{R_{iron}}} \tau_p r_{avg} C_l = 1.270309 mWb \tag{56}$$

while the measured mutual flux from the 3D model is $1.26643mWb$, which gives an error of 0.3%.

This shows that the 2D analytical model can be used to calculate the machine performance of this design. However, when there are armature current present in the machine, the air gap flux is reduced, as well as saturation effects in the lamination iron, which are not accounted for in the analytical approach and results in a larger error.

XVII. Analytical model with iron

In order to do quick calculations based on the design with laminated iron, an analytical model is created. The model is limited to 2D, calculated at average radius, assuming constant magnetic and electric loading on its active length. The equations are limiting the design to a single turn wave winding topology, similar to the prototype design. The wave winding is considered to be made of aluminum instead of copper, in order to reduce weight and costs. The rotor is not designed with Halbach array magnets, but rather conventional magnets with back iron.

The model input is the machine data, shown in table XII, where the rated performance of the machine is given. Further, the geometrical dimensions and material properties are needed, shown in table XIII and table XIV. From this, the geometric dependent variables are calculated, and then the number of coil layers in the stator, C_{lay}, the conductor axial depth, C_d, and magnet axial depth, M_d, to fit the electrical and magnetic loading defined by machine performance. As output, the torque constant, voltage constant, and efficiency are calculated, along with cost and weight of the active materials, and active axial length of the machine. The model has been tested with its corresponding geometry in 2D COMSOL, and provides a result within 5% error for various designs. A flow chart of the iron model can be seen in Fig. 83.

The application of this model is to find a design based on the given machine performance. Only the DC-losses are calculated, where the AC-losses, THD in the back-EMF waveform, and cogging must be calculated in a 3D FEM model when suitable design parameters from this model are set.

Most of the equations used in the iron free model can be reused, but the magnetic loading must be calculated analytically, and some new parameters are introduced.

A. Machine data

The machine data is shown in table XII, and acts as the rated performance in the model. The rated speed, induced voltage, current density, and torque are given here, along with the number of poles, phases, and multidisks. The calculations in the model is done for a double sided AFPM with interior stator topology, but multiplied with the number of multidisks to represent the entire motor.

The rated current density in this machine can be set very high. In the lab experiments by Lars Johan Clad [1], it is proved that with water cooling, the current density can be as high as $20A/mm^2$ with single side cooling, with $60°$ coil temperature. In this design, each stator layer will have a

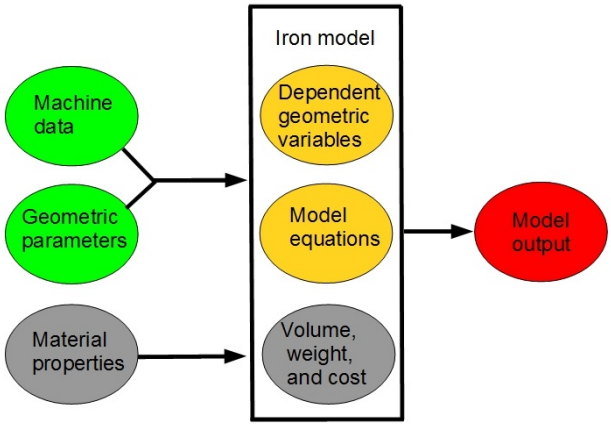

Fig. 83: Flow chart of the iron model

cooling duct at either side, enabling twice the cooling surface. Because of safety, the maximum current density is set to $20A/mm^2$.

The number of poles must be considered in combination with the lamination width and ratio of inner and outer diameter K_D, where the conductor width is restricting its range. A limit of $1mm$ conductor width at inner diameter is set.

The number of turns per phase per pole, $q = 1$, and number of phases, $ph = 3$, are restricted because of the model validation toward SolidWorks and COMSOL.

B. Geometric Parameters

The geometric parameters for the iron model are given in table XIII. It is convenient to have different diameter parameters for the inner and outer diameter for the active area of the stator, magnet, and back iron. For example, M_{Do} is "magnet outer diameter", and BI_{Do} is "back iron outer diameter". All axial lengths are denoted as "depth", for example BI_d is the "back iron axial depth".

The lamination width, L_w, and conductor width, C_w, are spanning the slot width. In this model, they are calculated from the amount of iron in the air gap surface area, R_{iron}, from (24) and (53).

Due to the reduction in eddy currents, the lamination axial depth is extended beyond the conducts, an extra variable is introduced to control the additional axial depth, denoted L_{ed}, "lamination extra depth".

The magnet remanence flux, B_r, is set to $1.3T$, which is the usual magnet strength available in the market today, while the magnet span, α_m, is set to 0.8 in accordance with the minimum THD calculated in section XI.

The material properties are given in table XIV, where the price, mass density, and the conductivity of the active materials are included.

C. Geometric dependent variables

The geometric dependent variables are calculated from the input geometry parameters in table XIII, their equations are given in table XV. The average radius, r_{avg}, is set to be in the middle of the active area of the stator coil, and used

TABLE XII:
Machine data

Description	Symbol	Unit
Rated rotational speed	n	rpm
Rated RMS induced voltage ph-n	E_{ph}	V
Rated RMS current density	J	A/mm^2
Rated total average torque	T_{tot}	Nm
Average air gap flux density	B_g	T
Number of stator poles	p	-
Number of turns per phase per pole	q	-
Number of phases	ph	-
Number of multidisk machines	M	-

TABLE XIII:
Geometric parameters

Description	Symbol	Unit
Stator active area outer diameter	C_{Do}	mm
Ratio between inner and outer stator diameter	K_D	$-$
Ratio between iron and air gap surface area	R_{iron}	-
Gap between stator layers	C_{layg}	mm
Lamination additional axial depth	L_{ed}	mm
Outer magnet diameter	M_{Do}	mm
Inner magnet diameter	M_{Di}	mm
Magnet remanence flux	B_r	
Ratio between magnet pitch and pole pitch	α_m	$-$
Back iron outer diameter	BI_{Do}	mm
Back iron inner diameter	BI_{Di}	mm
Air gap axial depth	g	mm

to calculate torque, back-EMF, and losses in the design. The accuracy of using average radius was shown in the previous section.

The back iron axial depth is dependent on the magnet width. The flux flowing through the magnet is divided into two, flowing in either direction in the back iron. The flux flowing in the back iron will therefore be half the air gap flux. By having the back iron axial depth a fourth of the magnet width, the flux density will become twice of the air gap flux density, which secures a high utilization of the iron.

D. Model equations

Once the geometric dependent variables are calculated, the design is set to be analyzed. The machine data is already given in the input parameters, but the model is suppose to calculate the number of coil layers and conductor axial depth, along with DC-resistance, efficiency, and volumetric, weight, and cost of the active materials. The equations are given in table XVII.

TABLE XIV:
Material properties

Description	Symbol	Value	unit
Aluminum conductivity	σ_{Al}	3.774e7	S/m
Aluminum specific weight	ρ_{Al}	2705	kg/m^3
Aluminum price	c_{Al}	4.62	NOK/kg
Magnet NdFeB conductivity	σ_m	6.25e5	S/m
Magnet NdFeB specific weight	ρ_m	7700	kg/m^3
Magnet NdFeB price	c_m	259.74	NOK/kg
Iron conductivity	σ_{Fe}	1.07e7	S/m
Iron specific weight	ρ_{Fe}	8000	kg/m^3
Iron price	c_{Fe}	12	NOK/kg

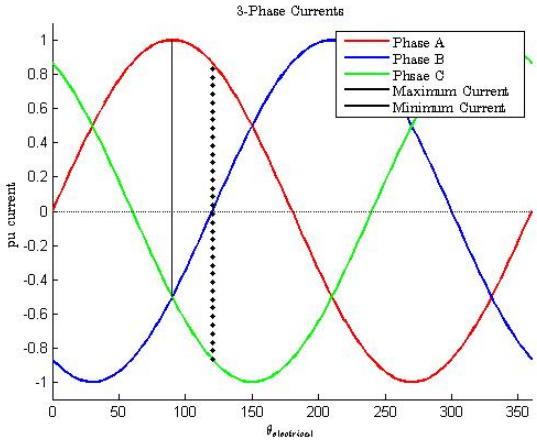

Fig. 84: Minimum and maximum electrical loading in a 3-phase system

The first step in the model is to calculate the number of turns needed to provide the rated back-EMF voltage using the average air gap flux density given as input. The back-EMF voltage for a single conductor situated in the iron slots are calculated as

$$\begin{aligned} e_{slot}(t) &= \frac{d\lambda}{dt} \\ &= \omega_{el} N \frac{d\Phi}{d\theta} \\ &= \omega_{el} N \hat{\Phi} cos(\theta) \\ &= \omega_{el} N \left[\int \int B_m(r,\theta) dA \right] cos(\theta) \end{aligned} \tag{57}$$

where the flux peak is calculated as shown in (56). The peak back-EMF voltage is then calculated as

$$\hat{e}_{slot} = \omega_{el} C_{lay} q \, B_g \tau_p r_{avg} C_l \tag{58}$$

where $N = C_{lay} q$, number of turns in a slot. The total phase RMS back-EMF is given in the input, and from that the number of stator layers are calculated

$$\begin{aligned} E_{ph} &= \frac{1}{\sqrt{2}} \hat{e}_{slot} p \, M \\ &= \frac{1}{\sqrt{2}} \omega_{el} C_{lay} q \, B_g \tau_p r_{avg} C_l p \, M \end{aligned} \tag{59}$$

$$C_{lay} = \sqrt{2} \frac{E_{ph}}{M} / \left(\omega_{el} q \, B_g \tau_p r_{avg} C_l p \right) \tag{60}$$

but due to the necessity of an integer number C_{lay}, the final equation is

$$C_{lay} = ceil \left[\sqrt{2} \frac{E_{ph}}{M} / \left(\omega_{el} q \, B_g \tau_p r_{avg} C_l p \right) \right] \tag{61}$$

When the number of layers are found, the axial depth of each layer is calculated from the minimum electrical loading to produce rated torque given in the input, using the average

air gap flux density and rated current density from the machine data. The electromagnetic torque from one conductor is calculated as

$$T = BILr_{avg} \tag{62}$$

The minimum amount of ampere-turns, NI, per pole, is calcuated as

$$NI = \frac{T_{tot}}{M\,p\,B_g C_l\ r_{avg}} \tag{63}$$

Using the minimum current, occuring at $\theta = 30°$, as shown in Fig 84, two phases are situated under the magnet, and producing $\sqrt{2}I_{ph}cos(\frac{\pi}{6})$ amperes in each. Using this as the minimum electrical loading, the ampere-turns can be calculated as

$$NI = C_{lay}q\,2\sqrt{2}I_{ph}cos(\frac{\pi}{6}) \tag{64}$$

The RMS phase current is calculated using the rated RMS current density and the average cross section of the conductor

$$I_{ph} = J\overline{C}_w C_d \tag{65}$$

The conductor cross section can then be calculated as

$$C_d = \frac{T_{tot}}{M} / \left(p\,B_g C_{lay} q\,2\sqrt{2}J\overline{C}_w cos(\frac{\pi}{6})C_l r_{avg}\right) \tag{66}$$

The magnet length is calculated from the rated air gap flux density using (51) and (55).

$$M_d = \frac{g}{\alpha_m \frac{B_r}{B_g} - 1}\frac{\alpha_m}{R_{iron}} \tag{67}$$

The DC resistances are calculated as described in the iron free model, which are still valid in this design, from equations (41), (42), and (43).

E. Volume, weight, and mass

The volumes of the active materials, back iron, magnets, laminations, and stator coils, are calculated as shown in table XVI. The volumes calculated in different designs has been compared to SolidWorks data, and shows a fairly good accuracy.

Only the active materials are available in this model to be calculated, but they are essential parts of the total machine. They are the main contributers to the bill of materials of the machine manufacturing costs, and gives an indication of the minimum cost of the design.

F. Model output

Now all motor dimensions are know, and the output variables can be calculated as shown in table XVIII. This model can be implemented in either Matlab or excel, but make sure that all geometrical dimensions are transformed from millimeters to meters when used in the equations.

The model can be looped, in order to do optimization of design, and can then be the initial parameter set to be linked with COMSOL through Matlab livelink, in order to perform 2D or 3D analysis.

From the master thesis of Lars Johan Clad, [1], an analytical model is created to find the HTC of the design, which can also be implemented in this model. Providing a very complex model which can be used to find suitable designs for the AFPM machine.

XVIII. Applications

The iron model presented in the previous chapter has been implemented in Excel in order to give some design examples. The main purpose of this machine is to be able to carry a large current density in its stator to enable a very torque dense machine. Since the conductor DC-losses are dependent on the phase current squared, while the torque output is proportional with the phase current, the efficiency will be very low. The AC-losses and rotational losses are not included in this model, but in a well designed motor these losses should be minimized to a neglectable level.

A. Capstan

The suitable situation for this design is a slow rotating and torque intense application, where hydraulic motors are used today. One example is a capstan, which are used for cargo handling and tightening mooring arrangements on board fishing or service ships. The typical requirement here is $6500Nm$ nominal torque, at $30rpm$ operating speed. The motor should be gear-less, indicating a high pole number. The diameter of the capstan is limited, and to be able to house the motor inside as the hydraulic motor, a multi-disk arrangement must be used.

The iron model input, calculations, and output are shown in Fig. 85. The result show that the torque requirement is met with five multi-disks and with 20 stator layers in each disk. The torque constant is $88.9Nm/A$, and a torque density at $67Nm/kg$. The efficiency is 35% at the rated speed, and the machine cost is $6500NOK$, and weighs $93kg$. The dimensions of the machine is about $400mm$ diameter with $33.8cm$ axial length. This is a very compact machine, but due to the limiting diameter, the axial length is relatively large.

B. Pancake machine

The ideal application for the AFPM design is where the axial length is restricted, giving a possibility to have a large diameter to enable a high torque. The industrial application can be from a large winch on ships, to elevator propulsion system. This design will limit the machine to a single disk motor, and as many poles as the geometry can handle. The outer coil diameter is set to $500mm$, and current density to $20A/mm^2$. The air gap flux density and amount of iron in stator, R_{iron}, is optimized to minimum machine axial length. The rated torque is set to the same as the previous example, giving a comparison between multi-disk and single disk design. The rated back-EMF voltage is set to $200V$ to ensure a terminal voltage within the $400V$ grid voltage at operating speed and load.

The model calculations can be seen in Fig. 86. The total axial length of the machine is $6.75mm$, with 29 coil layers, and $6.6mm$ long magnets. The axial depth of each layer is calculated to be $1mm$. The torque constant is calculated to be $70.2Nm/A$, which is expected since the torque and voltage

TABLE XV:
Dependent geometric variables

Description	Equation	Unit
Stator active area inner diameter	$C_{Di} = K_D C_{Do}$	mm
Stator active radial length	$C_l = \frac{C_{Do} - C_{Di}}{2}$	mm
Average coil radius	$r_{avg} = \frac{C_{Do} + C_{Di}}{4}$	mm
Pole pitch	$\tau_p = \frac{2\pi}{p}$	rad
Slot pitch	$\tau_s = \frac{\tau_p}{q\,ph}$	rad
Magnet pitch	$\tau_m = \alpha_m \tau_p$	rad
Average magnet width	$\overline{M}_w = \tau_m r_{avg}$	mm
Magnet radial length	$M_l = \frac{M_{Do} - M_{Di}}{2}$	mm
Back iron axial depth	$BI_d = \frac{\overline{M}_w}{4}$	mm
Lamination width	$L_w = 2 r_{avg} tan(\tau_s/2) R_{iron}$	mm
Average conductor width	$\overline{C}_w = 2 r_{avg}\, tan(\frac{\tau_s}{2})(1 - R_{iron})$	mm

TABLE XVI:
Volume, weight, and cost

Description	Equation	Unit
Mechanical rotational speed	$\omega_m = n\frac{2\pi}{60}$	rad/s
Electrical rotational speed	$\omega_{el} = \omega_m \frac{p}{2}$	rad/s
Number of stator layers	$C_{lay} = ceil\left[\sqrt{2}\frac{E_{ph}}{M} / \left(\omega_{el} q\, B_g \tau_p r_{avg} C_l p\right)\right]$	$-$
Axial depth of coil layer	$C_d = \frac{T_{tot}}{M} / \left(p\, B_g C_{lay} q\, 2\sqrt{2} J \overline{C}_w cos(\frac{\pi}{6}) C_l r_{avg}\right)$	mm
Magnet axial depth	$M_d = \frac{g}{\alpha_m \frac{B_r}{B_g} - 1} \frac{\alpha_m}{R_{iron}}$	mm
Stator active axial depth	$C_{totd} = C_{lay}(C_d + C_{layg}) - C_{layg}$	mm
Lamination total axial depth	$L_d = C_{totd} + 2L_{ed}$	mm
Stator active coil resistance	$R_{active} = \frac{C_l}{\sigma_{Al} \overline{C}_w C_d} p\, C_{lay}\, q$	Ω
Upper end coil resistance	$R^{upper}_{end-coil} = \frac{6\tau_s D_o/2}{\sigma_{Al} \overline{C}_w C_d/2} p/2 C_{lay} q$	Ω
Lower end coil resistance	$R^{lower}_{end-coil} = \frac{6\tau_s D_i/2}{\sigma \overline{C}_w C_d/2} p/2 C_{lay} q$	Ω
Phase neutral coil resistance	$R_{DC} = M(R_{active} + R^{upper}_{end-coil} + R^{upper}_{end-coil})$	Ω

level are similar to the latter example, but the torque density is now $159.61 Nm/kg$. The cost of the machine is $1850 NOK$, which is the third of the multi-disk arrangement, and weighs $40 kg$.

The resistive losses in this machine is in the area of $50 kW$, which is a challenge to handle. But the machine has 29 coil layers, and with a cooling duct between each layer, the cooling surface will be very large. Dividing the power loss on the available cooling surface, it yields to $9.25 mW/mm^2$, which is much lower than the HTC found during the lab testing.

XIX. Conclusion

The performance of the novel coil design has been described. The use of water-cutting introduces a variable conductor width which gives higher fill factor than other wire wounded topologies. The solid conductors along with a flat coil assembly gives access to very high current densities, and the resulting compactness may compete with hydraulic motor applications. The flat coil assembly provide a very flat machine design, and can give extremely high torque densities.

Several topologies and design suggestions with laminated iron has been presented, and the effects of cogging and THD in the back-EMF waveform has been investigated. Showing that with a large q, they can easily be reduced and neglected. However, for its simplicity and easy assemble, the single turn wave winding was chosen for the further work in this thesis.

A prototype has been designed, manufactured, assembled,

Machine data		
Symbol	Value	Unit
n	30	rpm
Eph	250	V
J	10	A/mm^2
Ttot	6250	Nm
Bg	0.875	T
p	40	
q	1	
ph	3	
M	5	

Geometric parameters		
Symbol	Value	Unit
C_Do	360	mm
K_D	0.6	
Riron	0.4	
Clayg	0.5	mm
Led	1	mm
M_Do	363.6	mm
M_Di	213.84	mm
Br	1.3	T
am	0.8	
BI_Do	367.236	mm
BI_Di	211.7016	mm
g	1	mm

Geometric Dependent Variables		
Symbol	Value	Unit
C_Di	216	mm
Cl	72	mm
ravg	144	mm
tau_p	0.157	rad
tau_s	0.052	rad
tau_m	0.126	rad
Mw	18.096	mm
Ml	74.88	mm
Bld	4.524	mm
Lw	3.017	mm
Cw	4.525	mm

Model equations		
Symbol	Value	Unit
omega_m	3.142	rad/s
omega_el	62.832	rad/s
Clay	20	
Cd	1.554	mm
Md	10.606	mm
Ctotd	40.578	mm
Ld	42.578	mm
Ract	0.21706	Ohm
RendUp	0.17048	Ohm
RendLow	0.10229	Ohm
Rcd	2.44912	Ohm

Output equations		
Symbol	Value	Unit
Iph	70.31	A
Vt	422.21	V
Pdc	36325.78	W
Pout	19634.95	W
nabla	35.09	%
motor_W	93.24	kg
motor_C	6442.34	NOK
motor_d	33.80	cm
K_T	88.89	Nm/A
K_M	67.03	Nm/kg
K_E	8.33	V/rpm

Fig. 85: Capstan design

Machine data		
Symbol	Value	Unit
n	30	rpm
Eph	200	V
J	20	A/mm^2
Ttot	6250	Nm
Bg	0.75561716	T
p	60	
q	1	
ph	3	
M	1	

Geometric parameters		
Symbol	Value	Unit
C_Do	500	mm
K_D	0.55	
Riron	0.32	
Clayg	0.5	mm
Led	1	mm
M_Do	505	mm
M_Di	272.25	mm
Br	1.3	T
am	0.8	
BI_Do	510.05	mm
BI_Di	269.5275	mm
g	1	mm

Geometric Dependent Variables		
Symbol	Value	Unit
C_Di	275	mm
Cl	112.5	mm
ravg	193.75	mm
tau_p	0.105	rad
tau_s	0.035	rad
tau_m	0.084	rad
Mw	16.232	mm
Ml	116.375	mm
Bld	4.058	mm
Lw	2.164	mm
Cw	4.599	mm

Model equations		
Symbol	Value	Unit
omega_m	3.142	rad/s
omega_el	94.248	rad/s
Clay	29	
Cd	0.968	mm
Md	6.643	mm
Ctotd	42.069	mm
Ld	44.069	mm
Ract	1.16512	Ohm
RendUp	0.54227	Ohm
RendLow	0.29825	Ohm
Rcd	2.00564	Ohm

Output equations		
Symbol	Value	Unit
Iph	89.03	A
Vt	378.57	V
Pdc	47697.18	W
Pout	19634.95	W
nabla	29.16	%
motor_W	39.16	kg
motor_C	1844.43	NOK
motor_d	6.75	cm
K_T	70.20	Nm/A
K_M	159.61	Nm/kg
K_E	6.67	V/rpm

Fig. 86: Pancake AFPM

TABLE XVII:
Model equations

Description	Equation	Unit
Back iron volume	$V_{BI} = 2\pi[(\frac{BI_{Do}}{2})^2 - (\frac{BI_{Di}}{2})^2]BI_d$	m^3
Back iron weight	$W_{BI} = \rho_{Fe} V_{BI}$	kg
Back iron cost	$C_{BI} = c_{Fe} M_{BI}$	NOK
Lamination volume	$V_L = ph\,p\,q\,M\,L_w L_d C_l$	m^3
Lamination weight	$W_L = \rho_{Fe} V_L$	kg
Lamination cost	$C_L = c_{Fe} M_L$	NOK
Magnet volume	$V_M = M_d \overline{M}_w M_l p\,M$	m^3
Magnet weight	$W_M = \rho_m V_M$	kg
Magnet cost	$C_M = c_m M_M$	NOK
Stator active volume	$V_{aC} = C_l \overline{C}_w C_d C_{lay} q\,p\,ph$	m^3
Stator upper end coil volume	$V_{eC}^{upper} = 6\tau_s D_o/2\overline{C}_w C_d/2C_{lay} q\,p/2\,ph$	m^3
Stator lower end coil volume	$V_{eC}^{lower} = 6\tau_s D_i/2\overline{C}_w C_d/2C_{lay} q\,p/2\,ph$	m^3
Total stator coil volume	$V_C = M(V_{aC} + V_{eC}^{upper} + V_{eC}^{lower})$	m^3
Stator coil weight	$W_C = \rho_{Al} V_C$	kg
Stator coil cost	$C_C = c_{Al} M_C$	NOK

TABLE XVIII:
Model output

Description	Equation	Unit
Phase current RMS	$I_{ph} = J\,\overline{C}_w C_d$	A
Terminal voltage	$V_t = E_{ph} + R_{DC} I_{ph}$	V
DC power loss	$P_{DC} = 3R_{DC} I_{ph}^2$	W
Power out	$P_{out} = T_{tot}\omega_m$	W
Efficiency	$\eta = \frac{P_{out}}{P_{out}+P_{DC}}$	$-$
Total motor weight	$motor_W = M_{BI} + M_L + M_M + M_C$	kg
Total motor cost	$motor_C = C_{BI} + C_L + C_M + C_C$	NOK
Motor total axial length	$motor_d = M(L_d + 2g + 2M_d) + 2BI_d$	mm
Torque constant	$K_T = T_{tot}/I_{ph}$	Nm/A
Torque per mass	$T_M = T_{tot}/motor_W$	Nm/kg
Voltage constant	$K_E = E_{ph}/n$	V/rpm

and tested. The prototype is an internal stator AFPM iron free topology with $45°$ shifted Halback array magnets, developed in cooperation with the Shell Eco Marathon team. The prototype proved difficult to successfully insulate, the margins set in the design, was too small to fit the electric insulating tape. Larger machined cuts, with plastic fittings, and rounded corners -no sharp edges-, would ease the assembly and insulation work drastically.

The prototype was tested in laboratory, and the results was as anticipated. However, comparing the results from the analytical model and the laboratory test, showed that the air gap magnetic field was 70% of its predicted value. This error is might due to a too high remanence flux in the model, and that the effective airgap in the prototype became larger than predicted, because of difficulties when assembling the Halbach array.

The prototype stator has a fill factor of 90%, which is higher than any commercial machine today. However, due to large conductors and no iron in the stator, the prototype motor had very high eddy current losses, and was practically acting as a magnetic brake. This limited the laboratory testing to low speed, and due to limiting power supply, low phase current as well. The range of the laboratory testing was up to $40rpm$ at no load, and $180W$ from the power supply.

Throughout the work done in this thesis, SolidWorks has been used to draw and investigate the mechanical feasibility

of the design. A parameterized model, based on the wave-winded single turn topology, has been made, and has been a useful resource for the development of the prototype and analytical models.

The effects of having iron in the stator design has been discussed. The main positive effects are the reduction of magnet induced eddy current loss in the conducts, low cost machine due to a smaller effective airgap, hence, reduced magnet size, and the possibility of increased axial length of the stator, enabling high electric loading. The negative effect is the cogging effects, non-sinusoidal air gap magnetic flux, larger skin effect in conductors, and a more complex assembly. An analysis of the different phenomenas has been conducted, and showed that the negative effects can be handled and reduced to a suitable level. However, a more detailed analysis must be conducted to accurately calculate the additional losses.

An analytical model, predicting the performance and geometric size of the machine, has been developed and presented. The model is limited to DC-power loss only, but provides a quick method to find suitable designs for various applications. The model can be used as an initial state in a design process, where FEM-tools are added on to calculate the AC-losses and rotating losses in the machine.

Using the analytical model, two applications are presented in this thesis, one directed toward a limiting diameter restriction with a multi-disk arrangement, and one with restriction in the axial direction with a single stator topology. The calculation shows that high torque density is found in both designs, and provide a low cost electric alternative to hydraulic motors. The single stator topology with restricted axial length, is the most suitable application for the AFPM in the industry, where there are no other motor technologies available that can compete with this design.

XX. Future work

The best practice at this stage of the design process, would be to find a suitable design for an application, and do extensive analysis through FEM-tools. In this way, the AC-losses are found and accounted for, THD in back-EMF can be calculated, cogging reduction can be implemented, and losses due to harmonics can be studied. This requires that the design is analyzed in a 3D model, with a time dependent study. The different phenomenas can be studied one at a time, and simultaneously develop analytical equations to predict the influence on the machine, in that way gradually update the analytical model. If there are phenomenas that cannot be determined accurately by analytical approaches, the FEM-tool must be included in the analytical model to perform the calculations.

A prototype has been successfully manufactured and assembled. From this, a study should be done to identify the restraining boundaries of the geometric parameters. Other manufacturing and assembly alternatives must be investigated to find the range of feasible solutions of the design, and constraining boundaries should be implemented in the analytical model.

The heat test laboratory results shows that the HTC of the stator can be analytically determined [1]. By using COMSOL, the design given from the analytical model can be imported, and Joule Heating physics can be used to identify the peak temperature in the stator. From this, the analytical model should be included with predicting equations, and limit the maximum current density, and minimum cooling surface area. Since the HTC is highly flow dependent, the actual cooling of the machine cannot be determined unless a full scale prototype is built and tested.

When the analytical analysis of the machine design is finished, and a design is set, an optimization process should be conducted. It can be gradually built up, using the analytical model or a FEM-tool, where different cost functions are used to identify its sensitivity. A relative small optimization is required to find a suitable optimum based on performance and geometric properties, but to to find its absolute optimum including manufacturing and material costs, is time consuming and difficult. This motor is still in its development state, and a full optimization is excessive until a large scale production of the motor is initiated.

References

[1] Lars Johan Clad, "Cooling System for High Energy Efficient Electric Motors", Master Thesis, NTNU , Norway, 2013. Department of Energy and Process Engineering

[2] D. C. Hanselmann "Brushless Permanent Magnet Motor Design", McGraw-Hill, Inc, New York, 1994.

[3] D J Patterson, C W Brice, R A Dougal, D Kovuri "The "Goodness" of Small Contemporary Permanent Magnet Electric Machines" Proceecings of the 2003 IEEE International Electric Machines and Dries Conference , IEMDC '03 Madison, Wisconsin, June 2003

[4] Stud.tech J. O. Lindtjørn, "Calculation and Design of two types of Axial-Flux Permanent Magnet generators for a direct drive wind turbine application", ENO, NTNU, July 2004

[5] F. Caricchi, F. Crescimbi, O. Honorati, G. Bianco, E. Santini, "Performance of coreless-winding axial-flux permanent-magnet Generator With Power Output at 400 Hz, 300 r/min" IEEE transactions on industry applications, vol. 34 NO. 6 November/December 1998

[6] Price development of neodymium magnets, http://www.supermagnete.de/eng/faq/price Visited 10.12.2012

[7] A. R. Millnes, "Multi-Hundred Horsepower Permanent Magnet Brushless Disc Motors", in Record of the 9th Annual IEEE Applied Power Electronics Conferene and Exposition, APEC'94, pp 351-355

[8] Changes and trends for neodymium magnets. http://www.supermagnete.de/eng/faq/price Visited 08/12-2012

[9] Axial Flux Permanent Magnet Brushless Machines - gieras

[10] Performance Analysis of a Coreless Permanent Magnet Brushless Motor - gieras

[11] Lubna Nasrin, "Improved Version of Energy Efficient Motor for Shell Eco Marathon", Master Thesis, NTNU & KTH, Norway, October 2011.

[12] Patent on axial flux coil design, inventor: J.E. Brennvall, Applicant: Greenway Energy AS, J.E. Brennvall. Number: WO2012128646 at www.epo.org

[13] Anyuan Chen, Robert Nilssen, Arne Nysveen, "Harmonic Analysis and Comparison of the Back EMFs of Four Permanent Magnet Machines with Different Winding Arrangements", Electrical Machines and Systems, 2008. ICEMS 2008. International Conference on , vol., no., pp.3043-3048, 17-20 Oct. 2008

[14] Studer, C., Keyhani, A., Sebastian, T., Murthy, S.K., "Study of cogging torque in permanent magnet machines," Industry Applications Conference, 1997. Thirty-Second IAS Annual Meeting, IAS '97., Conference Record of the 1997 IEEE , vol.1, no., pp.42-49 vol.1, 5-9 Oct 1997

[15] Caricchi, F., Capponi, F.G., Crescimbini, F., Solero, L., "Experimental study on reducing cogging torque and core power loss in axial-flux permanent-magnet machines with slotted winding," Industry Applications

Conference, 2002. 37th IAS Annual Meeting. Conference Record of the , vol.2, no., pp.1295-1302 vol.2, 13-18 Oct. 2002
[16] 5 axis water-cutter technology: http://www.wardjet.com/5-axis.html Visited: 17.12.2012
[17] Discussion with Arne Nordmark aboute molding technology and industrial methods, SINTEF, Phone: 98283978. 03.10.2012
[18] Aluminum price variation: http://www.indexmundi.com/commodities/?commodity=aluminum Visited 18.12.2012
[19] Copper price variation: http://www.indexmundi.com/commodities/?commodity=copper Visited 18.12.2012
[20] Material properties of Aluminum: http://no.wikipedia.org/wiki/Aluminium Visited 18.12.2012
[21] Material properties of Copper: http://en.wikipedia.org/wiki/Copper Visited 18.12.2012
[22] R. Pai, D. J. Hargreaves, "Green Tribology", Green Energy and Technology 2012, pp 347-391. Online ISBN: 978-3-642-23681-5 Pub: Springer Berlin Heidelberg
[23] Heat transfer coefficient of water and air, http://www.engineeringtoolbox.com/overall-heat-transfer-coefficient-d_434.html Visited: 18.12.2012
[24] Marian K.Kazimierczuk "High-Frequency Magnetic Components", John Wiley & Sons, Ltd, 2009, ISBN: 978-0-470-71453-9
[25] Insulation tape used on prototype: 3M - 79 TAPE 12MM - TAPE, GLASS CLOTH, 12MM X 55MM, Farnell product number: 2135716, http://no.farnell.com/3m/79-tape-12mm/tape-glass-cloth-12mm-x-55m/dp/2135716
[26] John Ola Buøy, "Development of High Efficiency Axial Flux motor for Shell Eco-Marathon", Master Thesis, NTNU, Norway 2013 Department of Electric Power Engineering